

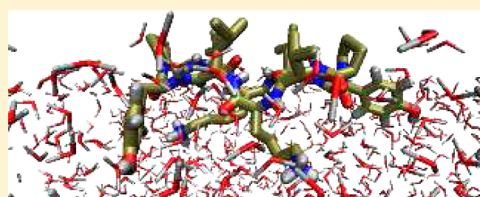


# Theoretical Sum Frequency Generation Spectroscopy of Peptides

Joshua K. Carr,\* Lu Wang, Santanu Roy, and James L. Skinner\*

Theoretical Chemistry Institute and Department of Chemistry, University of Wisconsin, Madison, Wisconsin 53706, United States

**ABSTRACT:** Vibrational sum frequency generation (SFG) has become a very promising technique for the study of proteins at interfaces, and it has been applied to important systems such as anti-microbial peptides, ion channel proteins, and human islet amyloid polypeptide. Moreover, so-called “chiral” SFG techniques, which rely on polarization combinations that generate strong signals primarily for chiral molecules, have proven to be particularly discriminatory of protein secondary structure. In this work, we present a theoretical strategy for calculating protein amide I SFG spectra by combining line-shape theory with molecular dynamics simulations. We then apply this method to three model peptides, demonstrating the existence of a significant chiral SFG signal for peptides with chiral centers, and providing a framework for interpreting the results on the basis of the dependence of the SFG signal on the peptide orientation. We also examine the importance of dynamical and coupling effects. Finally, we suggest a simple method for determining a chromophore’s orientation relative to the surface using ratios of experimental heterodyne-detected signals with different polarizations, and test this method using theoretical spectra.



## 1. INTRODUCTION

The biological activity of many proteins is intimately linked with their interactions with interfaces, most notably cellular membranes. For instance, antimicrobial peptides (AMPs), used by many organisms to defend against infection, may function by permeabilizing bacterial membranes.<sup>1,2</sup> A number of other peptides, such as voltage-gated ion channels, possess specialized structures that allow them to span the membrane.<sup>3</sup> Moreover, some peptides are thought to malfunction via membrane interactions; for example, the membrane interactions of human islet amyloid polypeptide (hIAPP) may be important to its aggregation, a process speculated to damage the membrane.<sup>4–6</sup>

Membrane-active proteins often function through a series of fast structural changes. To study them, therefore, it is desirable to employ an experimental technique that is selectively sensitive to the structure of interfacial proteins and that operates on the fast time scale of protein conformational change. Here, we describe just a few common techniques. One powerful technique for determining the structures of interfacial proteins in realistic environments is nuclear magnetic resonance, which has been used to probe many systems, including AMPs and proton channels in micelles and lipid membranes.<sup>1,7,8</sup> Electron paramagnetic resonance with site-specific spin labeling, meanwhile, has allowed researchers to examine particular elements of protein structure in detail and to characterize their dynamics, and has provided detailed information on protein conformational change in membranes.<sup>9,10</sup> Finally, infrared (IR) spectroscopic techniques provide a powerful means of studying protein structure and dynamics due to the sensitivity of vibrational line shapes to environmental influences and (for time-domain studies) due to the sub-picosecond periods of IR pulses, which enable these techniques to distinguish transient protein conformations. For example, linear and two-dimensional (2D) IR methods have been used to study the conformations of AMPs on a bilayer surface<sup>11</sup> and the

aggregation of hIAPP in the presence of lipid vesicles.<sup>12,13</sup> Attenuated total reflection Fourier transform IR spectroscopy provides additional interface selectivity due to the small penetration depth of the probe radiation, and it has been used to determine the orientation of membrane proteins.<sup>14–19</sup> Researchers using these techniques frequently employ detergent micelles or vesicles (instead of the native membrane) in order to create a soluble protein–lipid system, or remove excess solvent from a bilayer system.

Vibrational sum frequency generation (SFG) spectroscopy offers an attractive alternative to these techniques because of its intrinsic surface selectivity (described below), which obviates the need for vesicles or desolvated systems, and its fast dynamical time scale. Thus, it has become much-used for the study of interfacial proteins<sup>18–38</sup> and has enabled researchers to study these systems in real time and *in situ*.<sup>19,24,27,31–33,39–44</sup> In particular, many recent experiments have focused on the amide I (primarily CO-stretch) mode, which has also been extensively used for linear and 2D IR studies.<sup>11,13,45–51</sup> This mode is particularly attractive for proteins because it exhibits distinct spectral features for different secondary structures.<sup>17,27,52</sup>

In vibrational SFG spectroscopy, a resonant IR pulse and a non-resonant visible pulse are overlapped spatially and temporally on a sample surface, and the signal is detected at the sum frequency of the incident beams.<sup>20,53,54</sup> Typically, the pulses are controlled to propagate in a single plane (perpendicular to the sample surface), with polarizations either parallel (P) or perpendicular (S) to that plane, giving eight possible polarization combinations: PPP, PPS, PSP, SPP, PSS, SPS, SSP, and SSS (letters listed in decreasing frequency

**Special Issue:** Branka M. Ladanyi Festschrift

**Received:** August 4, 2014

**Revised:** September 9, 2014

**Published:** September 9, 2014

order—sum frequency, then visible, then IR). Within the dipole approximation, second-order nonlinear techniques such as SFG give no signal in centrosymmetric systems and are thus sensitive to interfaces, where centrosymmetry breaks. In systems of achiral molecules with random azimuthal orientation, the non-zero signals are SSP, SPS, PSS, and PPP;<sup>55,56</sup> these polarization combinations have been much-used in previous work on proteins.<sup>19,27,29,30,35–37,53,56–62</sup> In systems that additionally lack symmetry with respect to an arbitrary mirror plane perpendicular to the surface—e.g., randomly oriented chiral molecules—the SPP, PSP, and PPS signals can be non-zero as well.<sup>63,64</sup> SFG with these polarization combinations has thus been termed “chiral SFG”.<sup>32,64,65</sup>

Chiral SFG has been used to study interfacial proteins.<sup>18,27,32–34,65,66</sup> In particular, Yan and co-workers have found that different secondary structures can be distinguished on the basis of the existence of detectable PSP signals for the protein amide I and NH-stretch modes.<sup>33</sup> For example, a parallel  $\beta$ -sheet exhibited a distinct signal only for the amide I mode, an  $\alpha$ -helix exhibited a signal only for the NH-stretch mode, and an antiparallel  $\beta$ -sheet exhibited signals for both modes. Yan and co-workers have applied this method to monitor in real time the aggregation of hIAPP at a lipid membrane.<sup>32</sup> Chiral SFG thus holds great promise as a means for interfacial secondary structure determination.

Commonly, vibrational SFG spectra are interpreted in terms of a summation over independent contributions from amide vibrations in fixed orientations relative to the surface. That is, the amide I vibrations are described in terms of a limited number of local or normal modes; the local modes are assigned a fixed molecular-frame transition dipole and transition polarizability; and the protein is assumed to be fixed in a single conformation relative to the surface (i.e., the orientational distribution of each amide group is assumed to be a delta function).<sup>18–20,27,34,36,37,39,41,42,56,60,62,65–70</sup> Such a model may fail for three main reasons. First, vibrational coupling may cause the difference between the SFG signals of the local and normal modes to become significant. Second, peptide dynamics can alter the spectrum through effects such as motional narrowing (a decrease in line widths due to frequency self-averaging). Finally, even if coupling and dynamical effects can be ignored, the orientational distribution of the local amide modes is never truly a delta function.

In order to determine the relative importance of each of these factors, it is necessary to develop a theoretical framework within which experimental results may be interpreted. Several researchers have made strides in this direction for peptides, applying theory to static structures<sup>67,71</sup> or to relatively short (2 ns or less) simulations of fairly large proteins, whose SFG spectra are difficult to interpret in detail.<sup>72–74</sup> (It should be noted, however, that such short simulation times may actually be more justified for large proteins as opposed to smaller peptides, since large proteins tend to have stable structures that give rise to quickly converging spectra.) In this work, we take a different approach, using long (200 ns–1.25  $\mu$ s) molecular dynamics (MD) simulations to examine in detail both chiral and non-chiral SFG spectra for relatively small model systems.

In previous works, we have developed a theoretical strategy for the calculation of peptide amide I spectra from MD simulations and have applied this strategy to study, e.g., protein thermal unfolding and amyloid aggregation.<sup>46–49,51,75</sup> Here, we extend this method to the calculation of SFG spectra, providing a means to bridge SFG experiments and MD simulation, and to

interpret experimental spectra in a detailed manner. We then apply this method to study the SSP and PSP spectra of three model systems, which are displayed pictorially in Figure 1. First,

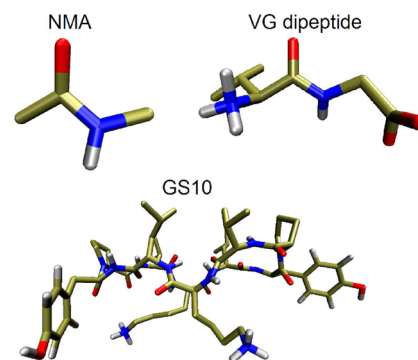


**Figure 1.** Model systems examined in this study. Carbon atoms are shown in tan, oxygen in red, nitrogen in blue, and hydrogen in silver. Note that aliphatic  $-\text{CH}$ ,  $-\text{CH}_2$ , and  $-\text{CH}_3$  groups are treated as united atoms in the force field, so these hydrogens are not shown.

we examine a single-chromophore achiral model amide, N-methylacetamide (NMA), in order to validate our spectroscopic model and to demonstrate a zero PSP signal for an achiral system. Next, we study a single-chromophore chiral molecule, VG dipeptide (in its zwitterionic form), and illustrate how the presence of a single chiral center gives rise to a significant PSP signal. We then calculate spectra for gramicidin S (GS10), a cyclic decapeptide with the sequence  $(\text{VKLYP})_2$ , which possesses overall  $C_2$  symmetry and a highly stable *anti*-parallel  $\beta$ -sheet structure.<sup>76–80</sup> Analysis of the results provides insight into the influence of secondary structure, vibrational coupling, and dynamics on SFG spectra. We conclude by suggesting a simple method for using ratios of experimental heterodyne-detected signals for different polarizations to determine a chromophore's orientation, and testing this method via our simulations.

## 2. METHODS

**2.1. Polarization Effects in Vibrational SFG.** In vibrational SFG, the sample interacts with a tunable IR beam with frequency  $\omega$  and polarization  $\hat{K}$ , and with a non-resonant visible beam with frequency  $\omega_{\text{vis}}$  and polarization  $\hat{J}$ . The signal is emitted with frequency  $\omega_S = \omega + \omega_{\text{vis}}$  and polarization  $\hat{I}$ , and is enhanced when the IR beam is resonant with a system vibration.<sup>53,54,81</sup> In Figure 2, we diagram the SFG setup. Typically, the scattering plane is perpendicular to the surface; we therefore define the Z-axis as the surface normal, and the X–Z plane as the scattering plane. The beams are polarized either in the X–Z plane (P polarization) or in the Y-direction (S polarization). The angles of the input and sum-frequency wavevectors with respect to the surface normal are  $\beta$ ,  $\beta_{\text{vis}}$ , and  $\beta_S$ ; by convention, we always consider the angle with respect to vectors pointing away from the surface, such that  $\beta$  is between 0 and  $90^\circ$  for all three beams. All these definitions apply to the laboratory frame, symbolized here using capital letters (X/Y/Z and I/J/K).

We now focus our derivation on the lab-frame SSP and PSP signals, which consist of three types of factors: elements of the (second-rank) Fresnel tensor  $\mathbf{L}$ , which describe effects caused by the different refractive indices of the media under study; factors arising from the angles of the input and sum-frequency

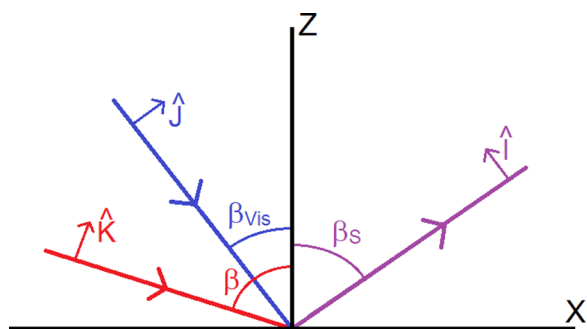


**Figure 2.** Diagram of the vibrational SFG setup.  $\hat{i}$ ,  $\hat{j}$ , and  $\hat{k}$  indicate the polarization directions for the sum frequency, visible, and IR beams, respectively (here drawn for PPP polarization).  $\beta_s$ ,  $\beta_{\text{vis}}$ , and  $\beta$  indicate angles relative to the surface normal. Subscript “S” indicates sum frequency and “vis” indicates visible; no subscript indicates IR.

beams; and elements of the complex third-rank tensor  $\chi$  (individual elements are symbolized as  $\chi_{IJK}$ ), which describe the intrinsic response of the sample.<sup>53,81–83</sup> ( $\chi$  is known as the second-order nonlinear susceptibility.) We symbolize the full lab-frame response (including all three effects) as  $\chi^{\text{eff}}$ , the “effective” response.  $\chi^{\text{eff}}$  is related to  $\chi$  by the equation<sup>56</sup>

$$\chi^{\text{eff}} = [\hat{I} \cdot \mathbf{L}(\omega_s, \beta_s)] : \chi : \{[\hat{J} \cdot \mathbf{L}(\omega_{\text{vis}}, \beta_{\text{vis}})][\hat{K} \cdot \mathbf{L}(\omega, \beta)]\} \quad (1)$$

To write the final expressions for the effective SSP and PSP signals,  $\chi_{\text{SSP}}^{\text{eff}}$  and  $\chi_{\text{PSP}}^{\text{eff}}$ , note that S-polarization corresponds to  $\hat{Y}$ -polarization in the lab frame, whereas P-polarization corresponds to polarization in the direction  $\cos \beta \hat{X} + \sin \beta \hat{Z}$  for the IR beam,  $\cos \beta_{\text{vis}} \hat{X} + \sin \beta_{\text{vis}} \hat{Z}$  for the visible beam, or  $-\cos \beta_s \hat{X} + \sin \beta_s \hat{Z}$  for the sum-frequency beam. Substituting these polarization vectors into eq 1 gives the results:

$$\begin{aligned} \chi_{\text{SSP}}^{\text{eff}} &= L_{YY}(\omega_s, \beta_s) L_{YY}(\omega_{\text{vis}}, \beta_{\text{vis}}) L_{XX}(\omega, \beta) \cos \beta \chi_{YYX} \\ &\quad + L_{YY}(\omega_s, \beta_s) L_{YY}(\omega_{\text{vis}}, \beta_{\text{vis}}) L_{ZZ}(\omega, \beta) \sin \beta \chi_{YYZ} \quad (2) \\ \chi_{\text{PSP}}^{\text{eff}} &= \\ &\quad -L_{XX}(\omega_s, \beta_s) L_{YY}(\omega_{\text{vis}}, \beta_{\text{vis}}) L_{XX}(\omega, \beta) \cos \beta_s \cos \beta \chi_{XXY} \\ &\quad -L_{XX}(\omega_s, \beta_s) L_{YY}(\omega_{\text{vis}}, \beta_{\text{vis}}) L_{ZZ}(\omega, \beta) \cos \beta_s \sin \beta \chi_{XXZ} \\ &\quad +L_{ZZ}(\omega_s, \beta_s) L_{YY}(\omega_{\text{vis}}, \beta_{\text{vis}}) L_{XX}(\omega, \beta) \sin \beta_s \cos \beta \chi_{ZZY} \\ &\quad +L_{ZZ}(\omega_s, \beta_s) L_{YY}(\omega_{\text{vis}}, \beta_{\text{vis}}) L_{ZZ}(\omega, \beta) \sin \beta_s \sin \beta \chi_{ZZZ} \quad (3) \end{aligned}$$

In this work, we will assume  $\beta = \beta_{\text{vis}} = 45^\circ$ ; because  $\omega_{\text{vis}} \gg \omega$  and  $\omega_s \sin \beta_s = \omega_{\text{vis}} \sin \beta_{\text{vis}} + \omega \sin \beta$ ,<sup>59</sup> we can also set  $\beta_s = 45^\circ$ . Within this limit, the angular terms merely contribute constant factors to both  $\chi_{\text{SSP}}^{\text{eff}}$  and  $\chi_{\text{PSP}}^{\text{eff}}$ , and we will ignore these factors.

Equations 2 and 3 can be simplified for systems with azimuthal symmetry (with respect to an arbitrary rotation around the Z-axis), such as those considered here. We therefore consider a “surface-fixed” frame, symbolized using lower-case letters ( $x/y/z$  and  $i/j/k$ ), for which  $\hat{Z} = \hat{z}$ , while the  $x$ - and  $y$ -axes have been rotated by an angle  $\tau$  such that  $\hat{X} = \cos \tau \hat{x} + \sin \tau \hat{y}$  and  $\hat{Y} = -\sin \tau \hat{x} + \cos \tau \hat{y}$ . Azimuthal symmetry is imposed by averaging over all angles  $\tau$ . Note that this causes all terms with an even number of Z-components to vanish, since these terms have an odd number of  $\sin \tau$  or  $\cos \tau$  factors when

converted into the surface-fixed frame.<sup>55</sup> Thus, azimuthal averaging gives the following results:

$$\begin{aligned} \chi_{\text{SSP}}^{\text{eff}} &\sim L_{YY}(\omega_s, \beta_s) L_{YY}(\omega_{\text{vis}}, \beta_{\text{vis}}) L_{ZZ}(\omega, \beta) \chi_{YYZ} \\ &= 0.5 L_{YY}(\omega_s, \beta_s) L_{YY}(\omega_{\text{vis}}, \beta_{\text{vis}}) L_{ZZ}(\omega, \beta) (\chi_{xxz} + \chi_{yyz}) \quad (4) \end{aligned}$$

$$\begin{aligned} \chi_{\text{SSP}}^{\text{eff}} &\sim -L_{XX}(\omega_s, \beta_s) L_{YY}(\omega_{\text{vis}}, \beta_{\text{vis}}) L_{ZZ}(\omega, \beta) \chi_{XZY} \\ &\quad + L_{ZZ}(\omega_s, \beta_s) L_{YY}(\omega_{\text{vis}}, \beta_{\text{vis}}) L_{XX}(\omega, \beta) \chi_{ZYX} \\ &= 0.5 L_{XX}(\omega_s, \beta_s) L_{YY}(\omega_{\text{vis}}, \beta_{\text{vis}}) L_{ZZ}(\omega, \beta) (\chi_{yxz} - \chi_{xyx}) \\ &\quad + 0.5 L_{ZZ}(\omega_s, \beta_s) L_{YY}(\omega_{\text{vis}}, \beta_{\text{vis}}) L_{XX}(\omega, \beta) (\chi_{zyx} - \chi_{zxy}) \\ &= 0.5 L_{ZZ}(\omega_s, \beta_s) L_{YY}(\omega_{\text{vis}}, \beta_{\text{vis}}) L_{XX}(\omega, \beta) (\chi_{zyx} - \chi_{zxy}) \quad (5) \end{aligned}$$

where the equality  $\chi_{yxz} = \chi_{xyx}$  though not true in general, is proven for our model in the next section. Because the Fresnel factors only contribute constant factors to both  $\chi_{\text{SSP}}^{\text{eff}}$  and  $\chi_{\text{PSP}}^{\text{eff}}$ , we now drop them as well. Defining the resulting quantities as simply  $\chi_{\text{SSP}}$  and  $\chi_{\text{PSP}}$ , we have

$$\chi_{\text{SSP}} \sim \chi_{xxz} + \chi_{yyz} \quad (6)$$

$$\chi_{\text{PSP}} \sim \chi_{zyx} - \chi_{zxy} \quad (7)$$

It is worth considering the effect of replacing  $\hat{Y}$  with  $-\hat{Y} = \sin \tau \hat{x} - \cos \tau \hat{y}$  in the above analysis. This amounts to performing a reflection across the X–Z plane. Because  $\chi_{\text{SSP}}^{\text{eff}}$  has two Y-polarized components, this reflection does not affect the SSP signal;  $\chi_{\text{PSP}}^{\text{eff}}$ , however, has only one such component, so this reflection will reverse the sign of the PSP signal. (The Fresnel and angular factors are not affected by this procedure.) Thus, for systems with reflection symmetry (i.e., achiral systems),  $\chi_{\text{PSP}}^{\text{eff}} = -\chi_{\text{PSP}}^{\text{eff}} = 0$ .

Note also that, due to the small time and length scales employed in simulated systems, azimuthal symmetry is not fully realized in our simulations. The experimental systems that we are attempting to model are azimuthally symmetric, however, and this ought to be reflected in the spectra. Accordingly, we identify the coordinate frame of the simulation not with the lab frame (X/Y/Z) but with the surface-fixed frame ( $x/y/z$ ), for which we impose azimuthal symmetry. (Hereafter, we will refer to this frame as the simulation frame.) Practically, this means that we calculate spectra using eqs 6 and 7, rather than eqs 2 and 3.

For GS10, we also calculate PPP spectra. The derivation for  $\chi_{\text{PPP}}$  is analogous to those for  $\chi_{\text{SSP}}$  and  $\chi_{\text{PSP}}$  and is presented in Appendix 1. Again ignoring the Fresnel and angular factors, the result is

$$\chi_{\text{PPP}} \sim -(\chi_{xxz} + \chi_{yyz}) + 2\chi_{zzz} \quad (8)$$

It should be noted that the justification for ignoring the Fresnel coefficients is not as strong here as for  $\chi_{\text{SSP}}$  and  $\chi_{\text{PPP}}$ ; see Appendix 1.

**2.2. Mixed Quantum/Classical Approach for Vibrational SFG.** In order to calculate SFG signals using eqs 6–8, we require a model for the second-order nonlinear susceptibility elements  $\chi_{ijk}$  in the simulation frame.  $\chi_{ijk}$  consists of both “resonant” (R) terms, which depend mostly on  $\omega$ , and “non-resonant” (NR) terms, which depend mostly on  $\omega_{\text{vis}}$ .<sup>53,81,83</sup> These are represented, respectively, as  $\chi_{ijk}^{\text{R}}(\omega)$  and  $\chi_{ijk}^{\text{NR}}(\omega_{\text{vis}})$ . In



this work, we focus exclusively on the heterodyne-detected signal, which is given by the imaginary part of  $\chi_{ijk}^R(\omega)$  and is the most physically meaningful part of the response.  $\chi_{ijk}^R(\omega)$  can be expressed as the following quantum time-correlation function (TCF):<sup>81</sup>

$$\chi_{ijk}^R(\omega) \sim i \int_0^\infty dt e^{i\omega t} \text{Tr}[\rho \alpha_{ij}(t) \mu_k(0)] \quad (9)$$

Here, the trace is over all nuclear quantum states,  $\rho$  is the equilibrium density operator for the nuclear Hamiltonian,  $\alpha_{ij}(t)$  is an element of the ground electronic state 1–0 transition polarizability tensor, and  $\mu_k(0)$  is an element of the 1–0 transition dipole. This equation represents  $\chi_{ijk}^R(\omega)$  as a quantum equilibrium statistical mechanical average, which is extremely difficult to evaluate for proteins in the condensed phase.

To simplify the analysis, we divide the system into a quantum subspace consisting of the amide I vibrations and a classical bath consisting of low-frequency modes (translations, rotations, and torsions).<sup>84–87</sup> Other high-frequency modes are ignored. We have previously applied such a mixed quantum/classical approach successfully to linear and 2D IR spectroscopy of liquid water<sup>88–93</sup> and peptides in aqueous solution and at lipid membranes,<sup>11,45–49,51,75,94</sup> as well as to SFG spectra of water at the liquid/air interface.<sup>81–83,95–97</sup> Within this approach, the susceptibility for a multi-chromophore system is given by<sup>83</sup>

$$\chi_{ijk}^R(\omega) \sim i \int_0^\infty dt e^{i\omega t} \sum_{pq} \langle a_{pij}(t) F_{pq}(t) m_{qk}(0) \rangle e^{-t/2T_1} \quad (10)$$

Here,  $p$  and  $q$  index the amide I chromophores, and  $a_{pij}(t)$  and  $m_{qk}(t)$  are the time-dependent 1–0 transition polarizability and transition dipole elements for chromophores  $p$  and  $q$ , respectively.  $T_1$  is the amide I first excited-state lifetime and is chosen to be 600 fs.<sup>98</sup> Importantly, the brackets now indicate an average over configurations from a classical MD simulation, making the calculation feasible.  $F(t)$  describes the time propagation of the Hamiltonian:

$$\dot{\mathbf{F}}(t) = -i\kappa(t)\mathbf{F}(t) \quad (11)$$

where  $\kappa(t)$  is the amide I Hamiltonian (divided by  $\hbar$ ):

$$\kappa_{pq}(t) = \omega_p(t)\delta_{pq} + \omega_{pq}(t)(1 - \delta_{pq}) \quad (12)$$

Here,  $\omega_p(t)$  is the time-dependent local mode frequency for chromophore  $p$ , and  $\omega_{pq}(t)$  is the time-dependent coupling between chromophores  $p$  and  $q$ .  $\delta_{pq}$  is the Kronecker delta.

To apply these equations, it is necessary to calculate  $\omega_p(t)$ ,  $\omega_{pq}(t)$ ,  $m_{qk}(t)$ , and  $a_{pij}(t)$  from an MD simulation. The calculation of the first three quantities has been described in previous works.<sup>48,99,100</sup> For proline frequencies and for modeling nearest-neighbor frequency shifts and couplings including proline, however, methods by Roy et al. are used.<sup>101</sup> To calculate  $a_{pij}(t)$ , we follow others<sup>60,72–74</sup> in employing the tensor determined by Tsuboi et al. for aspartame, a model amide.<sup>102</sup> In previous works, this tensor has been presented in its diagonal form; here, however, we present it in a molecular frame (symbolized using  $x'/y'/z'$ ) in which one of the axes is aligned with the transition dipole. (We do this so that the geometry of the chromophore in the simulation frame can be easily described using Euler angles of the transition dipole in the next section.) The transition dipole—which is modeled as a point dipole—has a location given by  $\vec{r}_C + (0.665 \text{ \AA})\hat{n}_{CO} + (0.258 \text{ \AA})\hat{n}_{CN}$ , where  $\vec{r}_C$  is the

position of the amide C, and  $\hat{n}_{CO}$  and  $\hat{n}_{CN}$  are unit vectors pointing from the amide C to the amide O and N, respectively. The dipole lies in the CON plane and forms an angle of  $10^\circ$  with the OC vector.<sup>99</sup> The molecular frame, then, is defined as follows:  $z'$  is aligned with the transition dipole;  $x'$  lies perpendicular to  $z'$  and in the CON plane such that the amide N has a positive  $x'$ -coordinate; and  $y'$  lies perpendicular to the CON plane so as to form a right-handed coordinate system. In this reference frame, depicted in Figure 3, the transition polarizability tensor is given by

$$\alpha = \begin{pmatrix} \alpha_{x'x'} & \alpha_{x'y'} & \alpha_{x'z'} \\ \alpha_{y'x'} & \alpha_{y'y'} & \alpha_{y'z'} \\ \alpha_{z'x'} & \alpha_{z'y'} & \alpha_{z'z'} \end{pmatrix} = \begin{pmatrix} 0.33235 & 0 & 0.29726 \\ 0 & 0.05 & 0 \\ 0.29726 & 0 & 0.86765 \end{pmatrix} \quad (13)$$

The equality  $\chi_{yxz} = \chi_{xyz}$  stated in the previous section, is a consequence of the symmetry of the transition polarizability tensor, specifically the fact that  $\alpha_{ij} = \alpha_{ji}$ . (Note that any rotation of this tensor, which can be represented as a unitary transformation, will preserve the symmetry of the tensor. Thus, the tensor is symmetric not only in the molecule-fixed frame, but in the simulation frame as well.)

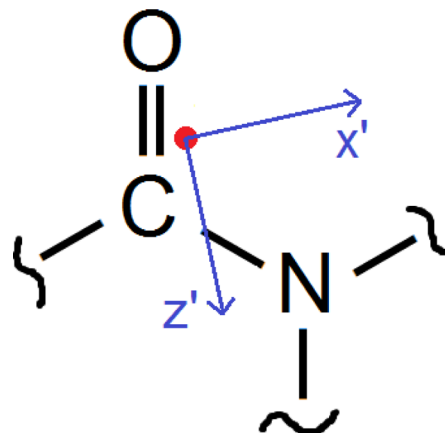


**Figure 3.** Diagram of the molecular frame Cartesian axes. The red dot signifies the location of the transition dipole. The  $z'$ -axis forms an angle of  $10^\circ$  with the OC vector, and the  $x'$  and  $z'$  axes are defined to lie in the CON plane. The  $y'$ -axis (not pictured) lies orthogonal to the CON plane so as to form a right-handed coordinate system.

**2.3. Effect of Orientation on SFG Amplitudes.** For later analysis, it is useful to consider the SFG spectrum of an isolated chromophore in the inhomogeneous limit (i.e., ignoring both coupling and dynamical effects). The isolated-chromophore version of eq 10 is<sup>81</sup>

$$\chi_{ijk}^R(\omega) \sim i \int_0^\infty dt e^{i\omega t} \langle a_{ij}(t) m_k(0) \exp(-i \int_0^t d\tau \omega(\tau)) \rangle e^{-t/2T_1} \quad (14)$$

In the inhomogeneous limit, the time dependence of the variables in the above expression is negligible, and we can replace  $a_{ij}(t)$  and  $\omega(\tau)$  with  $a_{ij}(0)$  and  $\omega(0)$ , respectively. If we ignore the lifetime decay (effectively letting  $T_1 \rightarrow \infty$ ), we can carry out the integration over  $t$ . We focus on the imaginary part of the result because we have chosen to examine the

heterodyne-detected signal. This gives us the SFG spectral density:

$$\text{Im } \chi_{ijk}^R(\omega) \sim \langle \delta(\omega - \omega(0)) a_{ij}(0) m_k(0) \rangle \quad (15)$$

For our model, the quantity  $a_{ij}(0)m_k(0)$  has no explicit frequency dependence, and it can be determined entirely from the geometry. Following an approach similar to that of Laaser and Zanni (among others),<sup>103</sup> we show in Appendix 2 that the value of  $a_{ij}(0)m_k(0)$  can be expressed in terms of two Euler angles: a tilt angle  $\theta$  that describes the angle between the transition dipole vector and the surface normal, and a twist angle  $\psi$  that describes a subsequent rotation around the transition dipole axis. (That a third angle is not required is a consequence of the azimuthal symmetry of the system.) We may therefore write

$$\begin{aligned} \text{Im } \chi_{ijk}^R(\omega) &\sim \langle \delta(\omega - \omega(0)) a_{ij}(\theta(0), \psi(0)) m_k(\theta(0), \psi(0)) \rangle \\ &= \langle \delta(\omega - \omega(0)) \int_0^\pi d\theta \int_0^{2\pi} d\psi \delta(\theta - \theta(0)) \delta(\psi - \psi(0)) A_{ijk}(\theta, \psi) \rangle \end{aligned} \quad (16)$$

where  $A_{ijk}(\theta, \psi) = a_{ij}(\theta, \psi) m_k(\theta, \psi)$ .

$A_{ijk}(\theta, \psi)$  is independent of the configurational average denoted by the angled brackets and can therefore be moved outside the average. We may also take the integrals outside the average, with the result:

$$\begin{aligned} \text{Im } \chi_{ijk}^R(\omega) &\sim \int_0^\pi d\theta \int_0^{2\pi} d\psi \langle \delta(\omega - \omega(0)) \delta(\theta - \theta(0)) \delta(\psi - \psi(0)) \rangle A_{ijk}(\theta, \psi) \\ &= \int_0^\pi d\theta \int_0^{2\pi} d\psi P(\omega, \theta, \psi) A_{ijk}(\theta, \psi) \end{aligned} \quad (17)$$

where  $P(\omega, \theta, \psi) = \langle \delta(\omega - \omega(0)) \delta(\theta - \theta(0)) \delta(\psi - \psi(0)) \rangle$  is the joint probability distribution describing the chromophore's frequency and orientation. Note that in the bulk, the orientational part of  $P(\omega, \theta, \psi)$  is isotropic and independent from the frequency distribution, such that  $P(\omega, \theta, \psi) = P(\omega) P(\theta, \psi) = P(\omega) \sin \theta / 4\pi$ .

Equation 17 provides a means of determining the effect of local-mode orientation on the SFG amplitude, independent of dynamic or coupling effects. To do this, we determine  $P(\omega, \theta, \psi)$  from simulation and use the following theoretical results (derived in Appendix 2) for  $A(\theta, \psi)$ :

$$\begin{aligned} A_{SSP}(\theta, \psi) &= 0.5(A_{xxz} + A_{yyz}) \\ &\sim (-0.2823 \sin^2 \theta \sin^2 \psi - 0.5945 \sin \theta \cos \theta \sin \psi \\ &\quad - 0.8177 \cos^2 \theta + 1.2000) \cos \theta \end{aligned} \quad (18)$$

$$\begin{aligned} A_{PSP}(\theta, \psi) &= 0.5(A_{zyx} + A_{zxy}) \\ &\sim 0.2973 \cos \psi \sin \theta \cos \theta + 0.2823 \sin \psi \cos \psi \sin^2 \theta \end{aligned} \quad (19)$$

$$\begin{aligned} A_{PPP}(\theta, \psi) &= -0.5(A_{xxz} + A_{yyz}) + A_{zzz} \\ &\sim (0.9970 \sin^2 \theta \sin^2 \psi + 0.1500 \sin^2 \theta \cos^2 \psi \\ &\quad + 1.7836 \sin \theta \cos \theta \sin \psi + 2.6030 \cos^2 \theta - 1.2500) \cos \theta \end{aligned} \quad (20)$$

Note that the numerical prefactors in the last two equations result from the substitution of values specific to our models of the amide I local mode transition dipole and polarizability. Thus, these equations apply only to amide I local modes treated using these models.

In Figure 4, we depict these results graphically. Note that whereas the SSP and PPP amplitudes depend mostly on the tilt angle  $\theta$ , the PSP amplitude depends more strongly on the twist angle  $\psi$ . Also, note that all three amplitudes are anti-symmetric on reflection over the line  $\theta = 90^\circ$ , followed by a  $180^\circ$  shift in  $\psi$ . This operation transforms  $\hat{x}'$  to  $-\hat{x}'$ ,  $\hat{y}'$  to  $-\hat{y}'$ , and  $\hat{z}'$  to  $-\hat{z}'$ ;

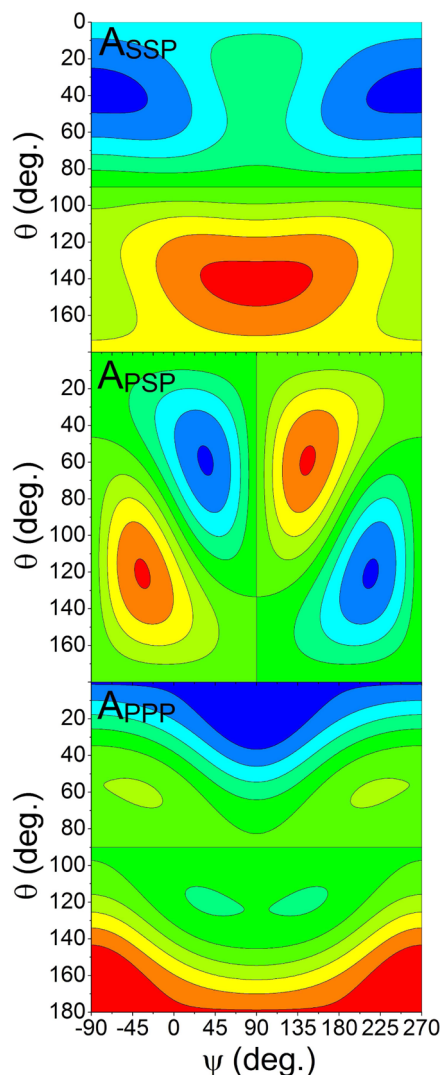


**Figure 4.** Theoretical SSP (top), PSP (middle), and PPP (bottom) amplitudes as a function of transition dipole orientation for the amide I model used in this study. Blue areas are positive, and red areas are negative. SSP contours run from a relative amplitude of  $-0.8$  to  $0.8$  in increments of  $0.16$ , PSP contours run from  $-0.25$  to  $0.25$  in increments of  $0.05$ , and PPP contours run from  $-1.64$  to  $1.64$  in increments of  $0.328$ .

i.e., it inverts the molecular orientation. Equivalently, we could replace  $A_{ijk}$  with  $A_{-i-j-k}$  which always reverses the sign because there are three Cartesian components.

A final important point concerns the fact that the SSP and PPP amplitudes are symmetric, and the PSP amplitude anti-symmetric, on reflection over the line  $\psi = 90^\circ$  or  $\psi = -90^\circ$ . The location of these lines of symmetry is a consequence of the fact that we chose the  $y'$ -axis to point out of the amide plane, such that for our model,  $\alpha_{x'y'} = \alpha_{y'z'} = 0$ , while  $\alpha_{x'z'}$  is non-zero. Because of this, a  $90^\circ$  rotation in  $\psi$  is required to align the amide plane (which for achiral molecules is the symmetry plane of the molecule) with the surface normal for arbitrary  $\theta$ . If we had instead chosen the  $x'$ -axis to point out of the amide plane, then  $\alpha_{y'z'}$  would have been the non-zero element, and the lines of symmetry would have been located at  $\psi = 0^\circ$  and  $\psi = 180^\circ$ .

**2.4. Calculation of Raman Spectra.** In this work, we calculate the Raman spectrum of dilute NMA in bulk water in order to verify the transferability of the transition polarizability tensor. Within the mixed quantum/classical approximation, the polarization-dependent Raman line shape for a single chromophore is given by<sup>92,104,105</sup>

$$I_{ij}(\omega) \sim \omega^4 \operatorname{Re} \int_0^\infty dt e^{i\omega t} \langle a_{ij}(t) a_{ij}(0) e^{-i \int_0^t d\tau \omega(\tau)} \rangle e^{-t/2T_1} \quad (21)$$

Typically, Raman spectra are recorded either in VV mode (input and signal polarizations parallel) or in VH mode (input and signal polarizations perpendicular). Due to the isotropy of the bulk system, the VV and VH spectra can be represented as spherical averages over the constituent  $I_{ij}$ 's:<sup>104</sup>

$$I_{VV} \sim \omega^4 \operatorname{Re} \int_0^\infty dt e^{i\omega t} \frac{1}{15} \sum_{ij=x,y,z} \langle [a_{ii}(0)a_{ij}(t) + 2a_{ij}(0)a_{ij}(t)] e^{-i \int_0^t d\tau \omega(\tau)} \rangle e^{-t/2T_1} \quad (22)$$

$$I_{VH} \sim \omega^4 \operatorname{Re} \int_0^\infty dt e^{i\omega t} \frac{1}{30} \sum_{ij=x,y,z} \langle [3a_{ij}(0)a_{ij}(t) - a_{ii}(0)a_{jj}(t)] e^{-i \int_0^t d\tau \omega(\tau)} \rangle e^{-t/2T_1} \quad (23)$$

The depolarization ratio is defined as<sup>106</sup>

$$Q = \frac{I_\perp}{I_\parallel} \quad (24)$$

where

$$I_\parallel = \int_0^\infty d\omega I_{VV} \quad (25)$$

$$I_\perp = \int_0^\infty d\omega I_{VH} \quad (26)$$

**2.5. Simulation Details.** MD simulations are performed according to the following procedure. First, the initial (cubic) box is constructed using the *genbox* utility of GRO-MACS4.5.3.<sup>107</sup> The box contains a single (*N*-deuterated) peptide of interest (NMA, VG, or GS10), sufficient water ( $D_2O$ ) molecules to fill a box with edge lengths of at least 4.05 nm (3004 for NMA, 2217 for VG, and 2354 for GS10), and, for GS10, two  $Cl^-$  counterions. This box is equilibrated in the NPT ensemble for at least 4 ns. Next, a continuation run is

performed in the NPT ensemble, and configurations are output every 100 ps so as to create an ensemble of 20 initial configurations for NMA, and 50 initial configurations for VG and GS10. For each of these configurations, a pair of surfaces is created by extending the  $z$ -dimension of the box to at least three times its initial size. Equilibration runs are then performed in the NVT ensemble for 5 ns for NMA and VG, and for 15 ns for GS10. Finally, NVT production runs are performed. For NMA, production runs are 10 ns in length, for a total simulation time of 200 ns; for VG, production runs are 25 ns, for a total of 1.25  $\mu s$ ; and for GS10, production runs are 20 ns, for a total of 1  $\mu s$ . Configurations for production runs are output every 10 fs.

For all runs, a 2 fs time step was employed, particle-mesh Ewald was used for electrostatics, and a simple cutoff with a long-range dispersion correction was applied for Lennard-Jones forces. Force-field parameters were taken from the GRO-MOS96 53a6 parameter set,<sup>108</sup> which employs the SPC water model.<sup>109</sup> For equilibration runs, the Berendsen thermostat and barostat<sup>110</sup> were used; for production runs, the Nosé–Hoover thermostat<sup>111,112</sup> was used.

Although GS10 remains at a single interface in all simulations, both NMA and VG cross the box and find the other interface on occasion; to address this, we apply a switching function to the transition dipole elements, as in previous work for water.<sup>96</sup> (The dipole elements are scaled based on the dipole position, as parametrized by Torii and Tasumi.<sup>99</sup>)

All reported spectra are averaged over the full length of the production runs, with starting points for the calculation of TCFs taken every 50 fs. All reported SFG spectra are normalized by the number of chromophores and the number of starting points used, such that the amplitudes of each are directly comparable.

### 3. RESULTS AND DISCUSSION

**3.1. Raman and SFG of NMA.** To investigate the transferability of the amide I transition polarizability tensor obtained for aspartame,<sup>102</sup> in Figure 5 we show VV and VH

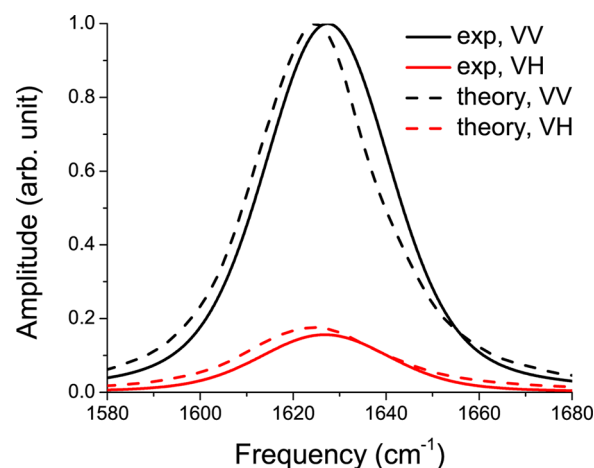


**Figure 5.** Experimental (solid) and theoretical (dashed) Raman VV (black) and VH (red) line shapes for bulk, aqueous *N*-deuterated NMA. Experimental curves are taken from Chen et al.<sup>106</sup> and are scaled to match the reported depolarization ratio of 0.16. Experimental and theoretical curves are also normalized to the maximum value for the VV line shape.

Raman spectra for bulk NMA in water, as well as experimental spectra from Chen et al.<sup>106</sup> The theoretical and experimental spectra compare favorably, and the theoretical depolarization ratio of 0.21 compares reasonably to the experimental value of 0.16 (see Table 4 from the experimental work<sup>106</sup>), considering that the theoretical tensor was taken from a different peptide.

In Figure 6, we show SSP and PSP line shapes for NMA (from the surface simulations). As significant statistical error is

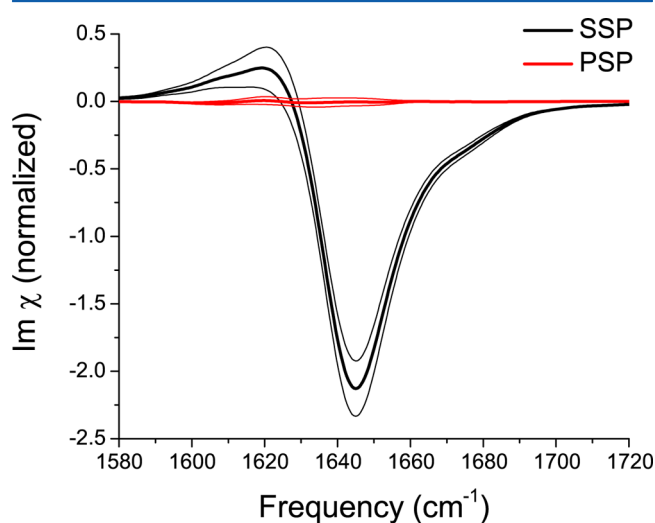


**Figure 6.** Theoretical SSP (black) and PSP (red) SFG spectra (imaginary part) for NMA. Thin lines mark the 95% confidence interval ( $\pm 2$  standard errors of the mean).

still present in our result even after 200 ns of MD, we also provide a 95% confidence interval for the results (thin lines), calculated by comparing the values for each frequency across the 20 independent runs. (This uncertainty, also present for VG dipeptide, seems to result mainly from the fact that NMA does not sit stably at one interface but ventures into the bulk and even crosses the box to find the other interface at several points in the simulations. Thus, portions of the simulation are spent not describing the interfacial configurations, but rather averaging over bulk configurations.) Note that the PSP signal for this achiral molecule is 0 (within the error), as expected. The interpretation of these results is fairly straightforward. NMA's frequency-dependent orientational distribution  $P(\omega, \theta, \psi)$  (determined from the MD simulations) is symmetrical on reflection over the line  $\psi = 90^\circ$  at all frequencies, such that its PSP signal vanishes (see Figure 4). The distribution is peaked near  $\theta = 90^\circ$ , but angles less than  $90^\circ$  are weakly favored at low frequency, while angles greater than  $90^\circ$  are favored somewhat more strongly at high frequency. Thus, although the peak in the frequency distribution  $P(\omega)$  is close to  $1625 \text{ cm}^{-1}$  (as in Figure 5), the SFG intensity is relatively weak at this frequency because the average  $\theta$  is very close to  $90^\circ$ . Instead, the SFG intensity peaks at  $\sim 1645 \text{ cm}^{-1}$ , where  $P(\omega)$  is smaller but a larger proportion of the transition dipoles point in the same direction (down).

To understand the frequency-dependent sign of the SSP signal, recall that in our model (taken from Torii and Tasumi<sup>99</sup>), the transition dipole points nearly opposite the CO bond vector. At low frequency, therefore, there is a slight tendency for the CO to point down. This favors the formation of hydrogen bonds between water and the carbonyl oxygen and lowers the amide I frequency. At high frequency, meanwhile,

the CO tends to point up, decreasing the number or strength of hydrogen bonds to water, and increasing the frequency.

**3.2. SFG of VG Dipeptide.** In Figure 7, we show SSP and PSP line shapes for VG dipeptide, again with 95% confidence

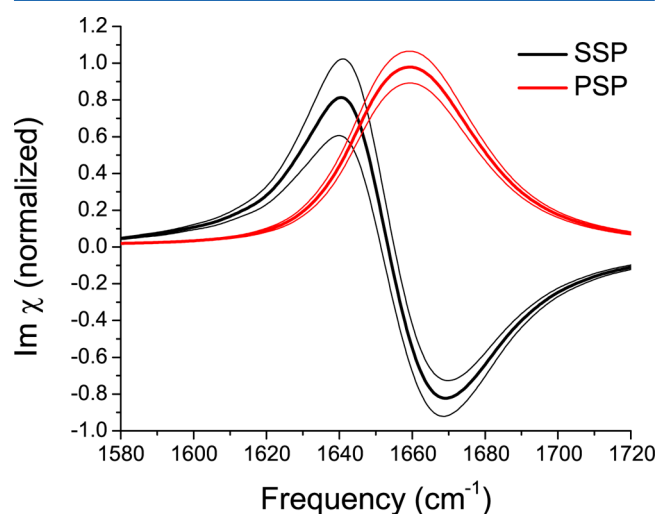


**Figure 7.** Theoretical SSP (black) and PSP (red) SFG spectra (imaginary part) for VG dipeptide. Thin lines mark the 95% confidence interval ( $\pm 2$  standard errors of the mean).

intervals. The SSP signal can be explained along similar lines as for NMA. VG differs in that it has a taller positive peak and a shallower negative peak, which may indicate that configurations with upward-pointing transition dipoles are overall more favorable in this case. Unlike NMA, the chiral VG molecule generates a significant PSP signal, which is roughly as intense as the SSP signal over the entire frequency range (in the limit that the Fresnel and angular factors are ignored). The presence and sign of the PSP signal can be understood from the fact that the transition dipole orientational distribution  $P(\theta, \psi)$  (again calculated from the simulation) is peaked near  $\theta = 95^\circ$ ,  $\psi = 195^\circ$ , in a region which Figure 4 shows to correspond to a positive PSP signal. Visualization of this geometry shows that it allows the carbonyl oxygen to point down, toward water, while allowing the valine side chain to point up, toward the vapor. Because of the chirality of the valine  $C^\alpha$ , the adoption of such a geometry requires specific tilt and twist angles. The PSP signal can therefore be readily understood from the geometric constraints imposed by the chirality of the molecule and the varying hydrophilicity of its parts.

**3.3. SFG of GS10.** Before showing spectra for GS10, it is worth describing its important structural features, as well as its typical orientation at the interface. GS10, a cyclic peptide with the sequence (VKLYP)<sub>2</sub>, effectively possesses  $C_2$  symmetry because the two VKLYP chains are structurally equivalent. (We say "effectively" because any given simulation snapshot is unlikely to show  $C_2$  symmetry; only the time-averaged structure does.) GS10 has a primarily anti-parallel  $\beta$ -sheet structure, with tight turns at the Pro side chains. The eight amide groups whose N is not donated by Pro (i.e., all except the amides arising from the Tyr–Pro peptide bond) form four cross-strand hydrogen bonds. At the interface, GS10 orients such that the Val and Leu side chains point toward the vapor, while the Lys and Tyr side chains point toward water. This interfacial configuration is quite stable, and the SFG spectra of GS10 are



well-converged after 1  $\mu$ s of simulation. Consequently, no confidence interval is shown for the SFG spectra of GS10.

In Figure 8, the SSP and PSP spectra for GS10 are shown (black), along with two limiting cases. In the first (red), the

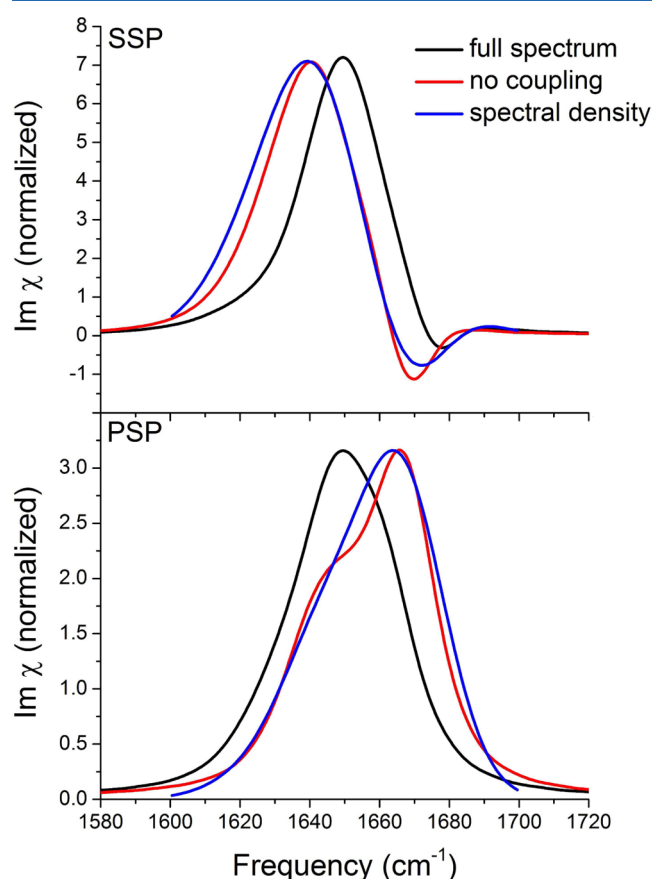


**Figure 8.** Theoretical SFG spectra (imaginary part, SSP and PSP) for GS10 peptide. Black line is the full calculation; red line is the calculation without coupling effects; blue line is the spectral density calculated using eq 17. Blue line is scaled to match the peak height of the red line.

spectrum is calculated with all couplings artificially set to zero. In the second (blue), the spectral density is calculated using eq 17 (summing over the individual results for each chromophore); this result is insensitive to both coupling and dynamical effects. Comparing the spectra with and without coupling (black and red), we see that coupling influences the spectra moderately: the peak positions shift by 10–15  $\text{cm}^{-1}$ , and the peak shape changes somewhat for the PSP spectrum. However, the influence of the coupling is small enough that the line shapes can be qualitatively explained without considering coupling effects. Meanwhile, comparing the line shape without coupling (red) to the spectral density (blue) reveals that dynamical effects such as motional narrowing have very little effect on the spectrum. Thus, to a very reasonable approximation, we can understand the SFG spectra simply in terms of the orientations of the individual amide I modes. For a significant signal to be observed, the amides must adopt orientations that not only give rise to large SFG amplitudes, but also do not significantly cancel each other. In GS10, for example, the SSP and PSP signals are strongly negative for only 2 of the 10 amides, causing the full-system SFG spectra to be mostly positive. The most important influence of secondary

structure, then, appears not to be its influence on the couplings between amides, but rather its influence on the relative orientation of the amides.

It is notable that the SFG spectra of GS10 lack the characteristic  $a^-$  and  $a^+$  peaks seen in the IR spectra of many  $\beta$ -peptides. For instance, the IR spectrum of the 12-residue  $\beta$ -hairpin Trpzip2 shows a low-frequency peak near  $1636\text{ cm}^{-1}$  and a high-frequency shoulder near  $1673\text{ cm}^{-1}$  in both experiment<sup>78</sup> and theory.<sup>48</sup> GS10's SFG spectra, however, lack a high-frequency shoulder. There are a few possible reasons for this. First, GS10 is even smaller than Trpzip2, and two of the four cross-strand hydrogen bonds (the ones nearest the turns) are somewhat unstable. Both of these factors will cause GS10's spectra to deviate from that of an idealized  $\beta$ -sheet. Second, the SFG spectrum includes contributions from both the transition dipole and the transition polarizability. Density functional theory calculations on a large  $\beta$ -sheet complex by Welch et al. indicate that the  $a^+$  mode of  $\beta$ -sheets is significantly less active in Raman spectroscopy than in IR spectroscopy,<sup>113</sup> which suggests that the transition polarizability associated with this mode is small.

**3.4. Determination of Individual Peptide Orientations Using SFG Spectra: Application to GS10.** In the previous sections, we have presented SFG spectra for model peptides and explained how their interfacial orientations—determined using simulation—give rise to the observed spectral features. It is also desirable to be able to determine peptides' orientations based simply on experimental data. To this end, it is common to employ a simplified model for the angular distribution, such that it is proportional to a two-dimensional delta function,  $\delta(\theta - \theta')\delta(\psi - \psi')$ . In this way, the problem of determining the angular distribution is reduced to the determination of two angles,  $\theta'$  and  $\psi'$ , a problem which can be solved using constraints from SFG or other techniques, such as linear dichroism.<sup>18–20,27,34,36,37,39,41,42,56,60,62,65–70</sup>

In the context of our formalism, within this approximation the triple joint distribution function is

$$P(\omega, \theta, \psi) = \tilde{P}(\omega, \theta', \psi')\delta(\theta - \theta')\delta(\psi - \psi') \quad (27)$$

If one is in the inhomogeneous limit, then from eq 17,

$$\text{Im } \chi_{ijk}^R(\omega) \sim \tilde{P}(\omega, \theta', \psi')A_{ijk}(\theta', \psi') \quad (28)$$

The important point is that if one forms the ratio of  $\text{Im } \chi$  for two different polarizations, then for a given frequency,  $\tilde{P}$  cancels and one obtains simply the ratio of the two  $A$  factors. For a given ratio of signals from two different polarizations, one can therefore use the expressions in eqs 18–20 to determine  $\theta', \psi'$  pairs that are consistent with this ratio. This generates iso-ratio curves in  $\theta$ – $\psi$  space. Because the SFG amplitudes depend on the frequency, data at different frequencies may produce different curves. Furthermore, various choices of the two polarizations lead to different functional forms for the ratio, generating different sets of curves. If the angular distribution is truly a delta function, then the curves for different polarization ratios will cross at certain points, which represent values of  $\theta$  and  $\psi$  consistent with the signal ratios. If the angular distribution is not a delta function (it never truly is) but is nevertheless sharply peaked, or if the spectral density expression of eq 17 is not an excellent approximation (because of motional narrowing), then the curves may not cross at the same point, but they should still approach each other.



In this section, we explore this idea by using the relative amplitudes of SSP, PSP, and PPP spectra of individual chromophore pairs in GS10 to determine constraints on those peptides' interfacial orientations consistent with a delta distribution. We examine chromophore pairs because the  $C_2$  symmetry of GS10 dictates that each peptide in GS10 has a counterpart whose environment is identical, on average. (E.g., the two chromophores derived from Val-Lys peptide bonds are structurally equivalent.) Moreover, analysis of the MD simulations reveals that the orientational distributions  $P(\theta, \psi)$  of each chromophore possess a single dominant peak, indicating that for the most part, the two amides sample similar orientations at any given time. This allows us to interpret the SFG spectra of each amide pair in terms of a single orientation.

In Figure 9, we present SSP, PSP, and PPP spectra (without coupling) for the amide pairs arising from the Val-Lys and

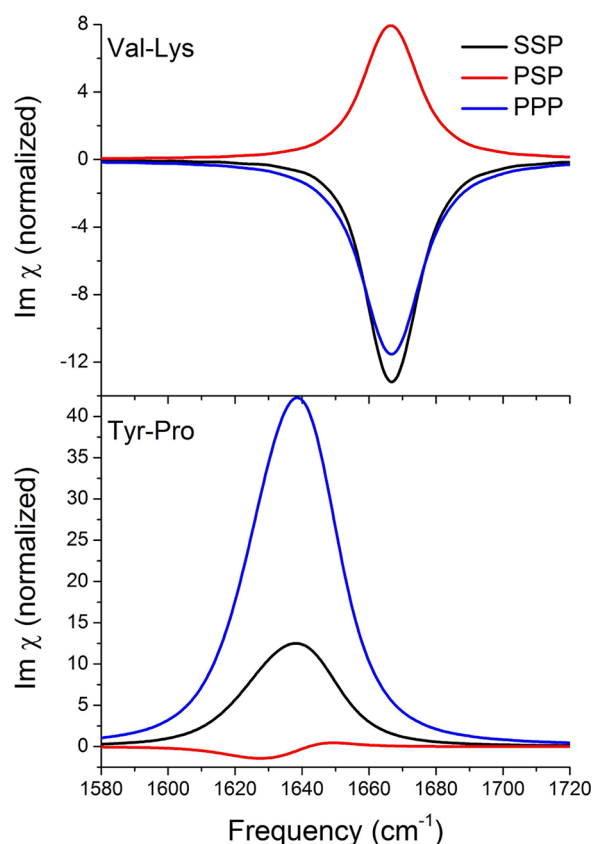


**Figure 9.** Theoretical SSP (black), PSP (red), and PPP (blue) spectra (imaginary part) including only chromophores from Val-Lys (top) or Tyr-Pro (bottom) peptide bonds. Coupling between the amide groups is not included.

Tyr-Pro peptide bonds. To analyze these spectra, we determine the amplitude ratios for PSP/SSP and PPP/SSP over a range of frequencies including the peak: 1650–1680  $\text{cm}^{-1}$  for Val-Lys (SSP peak at 1667  $\text{cm}^{-1}$ ), and 1620–1650  $\text{cm}^{-1}$  for Tyr-Pro (SSP peak at 1638  $\text{cm}^{-1}$ ). For Val-Lys, the PSP/SSP ratio varies from  $-0.787$  to  $-0.597$ , and the PPP/SSP ratio varies from  $0.887$  to  $1.353$ . For Tyr-Pro, the PSP/SSP ratio varies from  $-0.196$  to  $0.059$ , and the PPP/SSP ratio varies from  $3.105$  to  $3.399$ . As discussed above, each amplitude ratio is consistent with a line of constraint in  $\theta$  and  $\psi$ ; in Figure 10, these lines of constraint are plotted. Solid lines show orientations consistent with the PSP/SSP ratios, while dashed

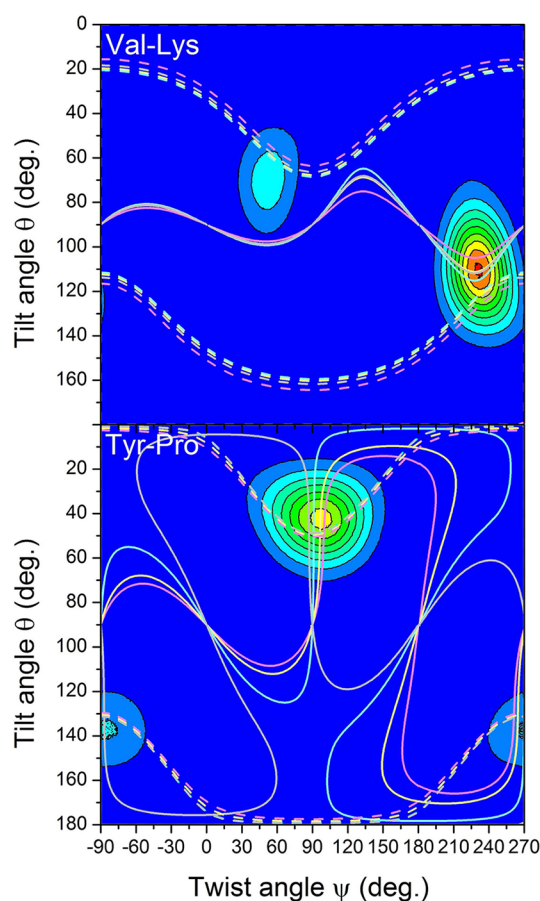


**Figure 10.** Transition dipole orientational distribution  $P(\theta, \psi)$  for Val-Lys (top) and Tyr-Pro (bottom) amides of GS10 at an air/water interface, along with lines of constraint derived by assuming a delta-function distribution consistent with the PSP/SSP (solid) and PPP/SSP (dashed) ratios at several frequencies. For orientational distributions, blue indicates low probability, and red indicates high probability. Val-Lys lines of constraint are determined at 1650 (magenta), 1660 (yellow), 1670 (cyan), and 1680 (gray); Tyr-Pro lines of constraint are determined at 1620 (magenta), 1630 (yellow), 1640 (cyan), and 1650 (gray).

lines show orientations consistent with the PPP/SSP ratios. Differently colored lines correspond to ratios determined at different frequencies.

For Val-Lys (top panel) one sees that there two regions in the  $\theta$ - $\psi$  plane where all the curves approach each other. Thus, this analysis yields two possible orientations consistent with the calculated spectra. However, we can rule out the solution near  $\theta = 65^\circ, \psi = 125^\circ$  because it corresponds to incorrect signs for the different signals. This leaves a single possible solution near  $\theta = 115^\circ, \psi = 235^\circ$ . We can now compare this predicted orientation with the actual orientational distribution, as determined by the simulation. This distribution is also shown in the top panel, and its dominant peak very nicely overlaps the region of the solution determined using SFG. A similar situation obtains for the Tyr-Pro chromophore pair (bottom panel). Again, although multiple solutions for the peptide orientation are possible, only one (the correct one, near  $\theta = 42^\circ, \psi = 98^\circ$ ) is consistent with the correct sign for each signal and with the data at each frequency.

Therefore, we conclude that for a single chromophore with a well-defined orientation, this method could be used to determine one or a few possible orientations from experimental

heterodyne-detected signals using at least three different polarizations (giving at least two amplitude ratios). In certain pathological situations, the method does not work well. For instance, the Leu–Tyr chromophore has an average tilt angle  $\theta$  very close to  $90^\circ$ , such that its SSP and PPP signals are small, and the SSP/PPP ratio does not offer a reliable constraint. Alternatively, if motional narrowing is important, or if the chromophore is not isolated (i.e., it has significant couplings to other chromophores), the results will worsen. Finally, there is the possibility that the angular distribution is not sharply peaked, in which case the method also will not work. Nonetheless, there would seem to be many instances in which the method will work well, especially if isotope-labeling is used to isolate single chromophores.

These results also emphasize the utility of examining the imaginary part of  $\chi$  (using heterodyne detection) rather than the magnitude of  $\chi$  (using homodyne detection). Because homodyned results lack sign information, they are not as useful for discriminating between multiple solutions that are consistent with the PSP/SSP and PPP/SSP ratios, making it necessary to use physical intuition or theoretical modeling to decide which result is correct.<sup>34,36,37,66,70</sup> Although such results are useful in many instances, it is of course desirable to use the most detailed information possible when interpreting experiments.

#### 4. CONCLUSIONS

In this study, we have presented a theoretical protocol for the calculation of peptide amide I SFG spectra (including “chiral” spectra) from MD simulations and applied it to study both achiral and chiral single-chromophore molecules, as well as a 10-amino-acid chiral peptide with an anti-parallel  $\beta$ -sheet secondary structure. We have shown that the SSP and PSP spectra of these model systems can be largely understood based simply on the orientational distributions of the amide I modes involved, with only minimal effects due to coupling or dynamics; indeed, such an approach has already been applied to static structures in previous studies (e.g., for the second harmonic generation spectra of bacteriorhodopsin<sup>114</sup>). This implies that the main roles of secondary structure in determining SFG amplitudes are simply to lock amide chromophores into tight orientational distributions and to determine whether the spectral contributions of different amide groups tend to reinforce or cancel each other.

For GS10, we made use of the PSP/SSP and PPP/SSP amplitude ratios to attempt to predict the amide orientations from the spectra by assuming a delta-function distribution for the orientation of the amides at the interface. This method typically yields tilt and twist angles consistent with the actual peak in the distribution. This suggests that as long as the orientational distribution is dominated by a single, relatively uniform peak, SFG amplitude ratios offer a reasonable means of determining the interfacial orientations of amide chromophores.

Despite some challenges, the development of experimental techniques for heterodyne detection and isotope labeling holds great promise for future studies in protein SFG spectroscopy. At present, most experiments employ homodyne detection, which, while simple and reasonably robust, does not permit the reliable extraction of the imaginary part of the resonant SFG signal; these experiments are thus difficult to compare to theoretical results, and do not provide a particularly strong basis for judging the accuracy of MD simulations. Heterodyne

detection, meanwhile, directly probes the imaginary part of the signal and thus allows for the extraction of detailed information related to the orientation of interfacial chromophores.<sup>115–119</sup> Meanwhile, isotope labeling provides a means of simplifying the SFG spectra of complex systems by shifting the frequencies of labeled chromophores away from the main amide I band.<sup>11,94,98,120–131</sup>  $^{13}\text{C}^{18}\text{O}$  labeling, for instance, typically lowers the amide I frequency by  $\sim 70\text{ cm}^{-1}$ . By isolating the spectral contributions of individual chromophores, their interfacial orientations can be probed even more directly by SFG.<sup>70</sup> Through the combination of these techniques with computational methods such as those outlined here, it becomes possible to obtain a detailed understanding of protein interactions with interfaces and to shed light on important processes such as the function of AMPs and ion channels or the aggregation of hIAPP.

#### ■ APPENDIX

##### 1. Simulation-Frame Expression for $\chi_{\text{PPP}}$

Evaluating eq 1 for the PPP polarization combination gives the result:

$$\begin{aligned}\chi_{\text{PPP}}^{\text{eff}} = & -L_{\text{XX}}(\omega_{\text{S}}, \beta_{\text{S}})L_{\text{XX}}(\omega_{\text{vis}}, \beta_{\text{vis}})L_{\text{XX}}(\omega, \beta) \\ & \cos \beta_{\text{S}} \cos \beta_{\text{vis}} \cos \beta \chi_{\text{XXX}} - L_{\text{XX}}(\omega_{\text{S}}, \beta_{\text{S}})L_{\text{XX}}(\omega_{\text{vis}}, \beta_{\text{vis}}) \\ & L_{\text{ZZ}}(\omega, \beta) \cos \beta_{\text{S}} \cos \beta_{\text{vis}} \sin \beta \chi_{\text{XXZ}} - L_{\text{XX}}(\omega_{\text{S}}, \beta_{\text{S}})L_{\text{ZZ}} \\ & (\omega_{\text{vis}}, \beta_{\text{vis}})L_{\text{XX}}(\omega, \beta) \cos \beta_{\text{S}} \sin \beta_{\text{vis}} \cos \beta \chi_{\text{XZX}} \\ & - L_{\text{XX}}(\omega_{\text{S}}, \beta_{\text{S}})L_{\text{ZZ}}(\omega_{\text{vis}}, \beta_{\text{vis}})L_{\text{ZZ}}(\omega, \beta) \\ & \cos \beta_{\text{S}} \sin \beta_{\text{vis}} \sin \beta \chi_{\text{ZZX}} + L_{\text{ZZ}}(\omega_{\text{S}}, \beta_{\text{S}})L_{\text{XX}}(\omega_{\text{vis}}, \beta_{\text{vis}})L_{\text{XX}} \\ & (\omega, \beta) \sin \beta_{\text{S}} \cos \beta_{\text{vis}} \cos \beta \chi_{\text{ZXX}} + L_{\text{ZZ}}(\omega_{\text{S}}, \beta_{\text{S}})L_{\text{XX}} \\ & (\omega_{\text{vis}}, \beta_{\text{vis}})L_{\text{ZZ}}(\omega, \beta) \sin \beta_{\text{S}} \cos \beta_{\text{vis}} \sin \beta \chi_{\text{ZZZ}} \\ & + L_{\text{ZZ}}(\omega_{\text{S}}, \beta_{\text{S}})L_{\text{ZZ}}(\omega_{\text{vis}}, \beta_{\text{vis}})L_{\text{XX}}(\omega, \beta) \\ & \sin \beta_{\text{S}} \sin \beta_{\text{vis}} \cos \beta \chi_{\text{ZZX}} + L_{\text{ZZ}}(\omega_{\text{S}}, \beta_{\text{S}})L_{\text{ZZ}}(\omega_{\text{vis}}, \beta_{\text{vis}})L_{\text{ZZ}} \\ & (\omega, \beta) \sin \beta_{\text{S}} \sin \beta_{\text{vis}} \sin \beta \chi_{\text{ZZZ}}\end{aligned}\quad (29)$$

Next, we transition to the surface-fixed (simulation) frame by making the substitutions  $\hat{X} = \cos \tau \hat{x} + \sin \tau \hat{y}$ ,  $\hat{Y} = -\sin \tau \hat{x} + \cos \tau \hat{y}$ , and  $\hat{Z} = \hat{z}$ , and averaging over all angles  $\tau$  (recall that this will cause all terms with an even number of Z-components to vanish):

$$\begin{aligned}\chi_{\text{PPP}}^{\text{eff}} \sim & -0.5L_{\text{XX}}(\omega_{\text{S}}, \beta_{\text{S}})L_{\text{XX}}(\omega_{\text{vis}}, \beta_{\text{vis}})L_{\text{ZZ}}(\omega, \beta) \\ & (\chi_{\text{xxz}} + \chi_{\text{yyz}}) - 0.5L_{\text{XX}}(\omega_{\text{S}}, \beta_{\text{S}})L_{\text{ZZ}}(\omega_{\text{vis}}, \beta_{\text{vis}})L_{\text{XX}}(\omega, \beta) \\ & (\chi_{\text{xxz}} + \chi_{\text{yyz}}) + 0.5L_{\text{ZZ}}(\omega_{\text{S}}, \beta_{\text{S}})L_{\text{XX}}(\omega_{\text{vis}}, \beta_{\text{vis}})L_{\text{XX}}(\omega, \beta) \\ & (\chi_{\text{zxx}} + \chi_{\text{zyy}}) + L_{\text{ZZ}}(\omega_{\text{S}}, \beta_{\text{S}})L_{\text{ZZ}}(\omega_{\text{vis}}, \beta_{\text{vis}})L_{\text{ZZ}}(\omega, \beta)\chi_{\text{zzz}}\end{aligned}\quad (30)$$

Since  $\omega_{\text{vis}} \approx \omega_{\text{S}}$  and  $\beta_{\text{vis}} \approx \beta_{\text{S}}$ , it is reasonable to assume that  $L_{\text{XX}}(\omega_{\text{S}}, \beta_{\text{S}})L_{\text{ZZ}}(\omega_{\text{vis}}, \beta_{\text{vis}}) \approx L_{\text{ZZ}}(\omega_{\text{S}}, \beta_{\text{S}})L_{\text{XX}}(\omega_{\text{vis}}, \beta_{\text{vis}})$ . In this case, the second and third terms cancel due to the symmetry of the transition polarizability tensor  $\alpha$ . The Fresnel components of the remaining (first and fourth) terms cannot rigorously be dropped, as they dictate the relative contributions of these terms to the PPP amplitude. However, accurately determining the Fresnel coefficients is difficult due to the need to quantify

an interfacial refractive index.<sup>59</sup> We therefore choose to ignore the Fresnel coefficients, and justify this choice as follows: (1) We do not attempt to compare to experimental data, and this choice introduces no inconsistency in our results. (2) The Fresnel coefficients typically do not differ drastically; for the air–water interface, for instance, substitution of reasonable values for the refractive indices of both media and the interface gives  $L_{xx} = 0.95$  and  $L_{zz} = 0.76$ .<sup>59</sup> Thus, although our results will certainly differ quantitatively from actual experimental data, we do not expect significant qualitative errors. Multiplying the result by 2 (as done for the SSP and PSP signals in the main text) yields eq 8:

$$\chi_{\text{PPP}} \sim -(\chi_{xxz} + \chi_{yyz}) + 2\chi_{zzz} \quad (31)$$

## 2. Expressions for SFG Amplitudes in Terms of Euler Angles

Equation 17 provides a means of determining the effect of local mode orientation on the SFG amplitude, independent of dynamical or coupling effects. The probability distribution  $P(\omega, \theta, \psi)$  can be determined from simulation. Here, we solve for the combinations of factors  $A_{ijk}(\theta, \psi) = a_{ij}(\theta, \psi)m_k(\theta, \psi)$  needed for the SSP, PSP, and PPP polarization combinations. To do this, we first define the Euler angles that describe the transformation from the simulation frame to the molecular frame (and thereby define the orientation of the amide in the simulation frame). Then, we express the relevant combinations of simulation-frame factors of  $A_{ijk}(\theta, \psi)$  in terms of molecular-frame parameters and Euler angles.

The Euler angles are defined by starting with the simulation frame ( $x/y/z$ ) and performing a series of rotations so as to bring this frame into alignment with the molecular frame ( $x'/y'/z'$ ). First, a counterclockwise rotation around the  $z$ -axis (looking down this axis) by an angle  $\phi$  is performed; then, a counterclockwise rotation around the new  $x$ -axis by an angle  $\theta$  (the tilt angle) is performed; finally, a counterclockwise rotation around the new  $z$ -axis by an angle  $\psi$  (the twist angle) is performed. This process is encapsulated mathematically by the following rotational matrix:<sup>132</sup>

$$\mathbf{R} = \begin{pmatrix} \cos \phi \cos \psi - & -\cos \phi \sin \psi - & \sin \phi \sin \theta \\ \sin \phi \cos \theta \sin \psi & \sin \phi \cos \theta \cos \psi & \\ \sin \phi \cos \psi + & -\sin \phi \sin \psi + & -\cos \phi \sin \theta \\ \cos \phi \cos \theta \sin \psi & \cos \phi \cos \theta \cos \psi & \\ \sin \theta \sin \psi & \sin \theta \cos \psi & \cos \theta \end{pmatrix} \quad (32)$$

The transition polarizability tensor  $\alpha$  defined in eq 13 is equal to the simulation-frame tensor  $\mathbf{a}$  if the simulation and molecular frames are aligned. To determine the polarizability tensor for an arbitrary orientation of the molecular frame, then, we perform the unitary transformation,

$$\mathbf{a} = \mathbf{R} \alpha \mathbf{R}^T \quad (33)$$

The form of the transition dipole vector is simpler because we have chosen this vector to coincide with the molecular-frame  $z'$ -axis. Ignoring the transition dipole magnitude (which only scales the results by a constant factor), the simulation-frame transition dipole is given by

$$\hat{\mu} = \begin{pmatrix} \sin \phi \sin \theta \\ -\cos \phi \sin \theta \\ \cos \theta \end{pmatrix} \quad (34)$$

To generate the geometric factors  $A_{\text{SSP}}(\theta, \psi)$  and  $A_{\text{PSP}}(\theta, \psi)$ , we simply substitute the appropriate elements of  $\alpha$  and  $\hat{\mu}$  for each factor  $A_{ijk}(\theta, \psi)$ , following eqs 6 and 7. Symbolically, this yields

$$\begin{aligned} A_{\text{SSP}}(\theta, \psi) &= 0.5(A_{xxz} + A_{yyz}) \sim (a_{xx} + a_{yy})\mu_z \\ &= \sum_{i,j=x,y,z} (R_{xi}\alpha_{i'j'}R_{xj} + R_{yi}\alpha_{i'j'}R_{yj})\mu_z \\ &= [(\alpha_{y'y'} - \alpha_{x'x'}) \sin^2 \theta \sin^2 \psi \\ &\quad - 2\alpha_{x'z'} \sin \theta \cos \theta \sin \psi + (\alpha_{y'y'} - \alpha_{z'z'}) \\ &\quad \cos^2 \theta + (\alpha_{x'x'} + \alpha_{z'z'})] \cos \theta \end{aligned} \quad (35)$$

$$\begin{aligned} A_{\text{PSP}}(\theta, \psi) &= 0.5(A_{zyx} + A_{zxy}) \sim a_{zy}\mu_x - a_{zx}\mu_y \\ &= \left( \sum_{i,j=x,y,z} R_{zi}\alpha_{i'j'}R_{yj} \right) \mu_x - \left( \sum_{i,j=x,y,z} R_{zi}\alpha_{i'j'}R_{xj} \right) \mu_y \\ &= (\alpha_{x'x'} - \alpha_{y'y'}) \sin^2 \theta \sin \psi \cos \psi \\ &\quad + \alpha_{x'z'} \sin \theta \cos \theta \cos \psi \end{aligned} \quad (36)$$

$$\begin{aligned} A_{\text{PPP}}(\theta, \psi) &= -0.5(A_{xxz} + A_{yyz}) + A_{zzz} \\ &\sim -(a_{xx} + a_{yy})\mu_z + 2a_{zz}\mu_z \\ &= - \sum_{i,j=x,y,z} (R_{xi}\alpha_{i'j'}R_{xj} + R_{yi}\alpha_{i'j'}R_{yj})\mu_z \\ &\quad + 2 \sum_{i,j=x,y,z} R_{zi}\alpha_{i'j'}R_{zj} \\ &= [3\alpha_{x'x'} \sin^2 \theta \sin^2 \psi \\ &\quad + 6\alpha_{x'z'} \sin \theta \cos \theta \sin \psi \\ &\quad + 3\alpha_{y'y'} \sin^2 \theta \cos^2 \psi + 3\alpha_{z'z'} \cos^2 \theta \\ &\quad - (\alpha_{x'x'} + \alpha_{y'y'} + \alpha_{z'z'})] \cos \theta \end{aligned} \quad (37)$$

(In deriving these results, we have assumed that  $\alpha_{x'y'} = 0$  and  $\alpha_{y'z'} = 0$ , as is the case for our amide I model.) It is interesting to note that if  $\alpha_{x'x'} = \alpha_{y'y'}$  and  $\alpha_{x'z'} = 0$ , the PSP signal is zero. These conditions are fulfilled for bond polarizability models (models of  $\alpha$  possessing cylindrical symmetry) when the unique principal axis of the transition polarizability is aligned with the transition dipole. The anisotropy of  $\alpha$  is thus critical to the observation of a sizable PSP signal.

Substituting values for the transition polarizability elements according to eq 13 gives the numerical results for  $A(\theta, \psi)$  listed in eqs 18–20. Note that the numerical prefactors in eqs 18–20 result from the substitution of values specific to our models of the amide I local mode transition dipole and polarizability. Thus, these equations apply only to amide I local modes treated using these models. In particular, the normal modes of multi-chromophore systems do not have the same  $\alpha$  and  $\hat{\mu}$  as the local modes from which they are composed; therefore, these equations apply to multi-chromophore systems only in the limit that couplings are ignored.



## ■ AUTHOR INFORMATION

## Corresponding Authors

\*E-mail: jcarr@chem.wisc.edu.

\*E-mail: skinner@chem.wisc.edu.

## Notes

The authors declare no competing financial interest.

## ■ ACKNOWLEDGMENTS

This work was supported by NIH grant 1R01DK088184 to J.L.S.

## ■ REFERENCES

- (1) Brogden, K. A. Antimicrobial Peptides: Pore Formers or Metabolic Inhibitors in Bacteria? *Nat. Rev. Microbiol.* **2005**, *3*, 238–250.
- (2) Mátyus, E.; Kandt, C.; Tieleman, D. P. Computer Simulation of Antimicrobial Peptides. *Curr. Med. Chem.* **2007**, *14*, 2789–2798.
- (3) Nelson, D. L.; Cox, M. M. *Lehninger Principles of Biochemistry*; W. H. Freeman and Co.: New York, 2005.
- (4) Clark, A.; Cooper, G. J. S.; Lewis, C. E.; Morris, J. F.; Willis, A. C.; Reid, K. B. M.; Turner, R. C. Islet amyloid formed from diabetes-associated peptide may be pathogenic in type-2 diabetes. *Lancet* **1987**, *2*, 231–234.
- (5) Lorenzo, A.; Razzaboni, B.; Weir, G. C.; Yankner, B. A. Pancreatic Islet Cell Toxicity of Amylin Associated with Type-2 Diabetes Mellitus. *Nature* **1994**, *368*, 756–760.
- (6) Chiti, F.; Dobson, C. M. Protein Misfolding, Functional Amyloid, and Human Disease. *Annu. Rev. Biochem.* **2006**, *75*, 333–366.
- (7) MacKenzie, K. R.; Pretegard, J. H.; Engelman, D. M. A Transmembrane Helix Dimer: Structure and Implications. *Science* **1997**, *276*, 131–133.
- (8) Cady, S. D.; Schmidt-Rohr, K.; Wang, J.; Soto, C. S.; DeGrado, W. F.; Hong, M. Structure of the Amantadine Binding Site of Influenza M2 Proton Channels in Lipid Bilayers. *Nature* **2010**, *463*, 689–692.
- (9) Hubbell, W. L.; Cafiso, D. S.; Altenbach, C. Identifying Conformational Changes with Site-Directed Spin Labeling. *Nat. Struct. Biol.* **2000**, *7*, 735–739.
- (10) Perozo, E.; Kloda, A.; Cortes, D. M.; Martinac, B. Physical Principles Underlying the Transduction of Bilayer Deformation Forces During Mechanosensitive Channel Gating. *Nat. Struct. Biol.* **2002**, *9*, 696–703.
- (11) Woys, A. M.; Lin, Y.-S.; Reddy, A. S.; Xiong, W.; de Pablo, J. J.; Skinner, J. L.; Zanni, M. T. 2D IR Line Shapes Probe Ovispirin Peptide Conformation and Depth in Lipid Bilayers. *J. Am. Chem. Soc.* **2010**, *132*, 2832–2838.
- (12) Ling, Y. L.; Strasfeld, D. B.; Shim, S.-H.; Raleigh, D. P.; Zanni, M. T. Two-Dimensional Infrared Spectroscopy Provides Evidence of an Intermediate in the Membrane-Catalyzed Assembly of Diabetic Amyloid. *J. Phys. Chem. B* **2009**, *113*, 2498–2505.
- (13) Middleton, C. T.; Buchanan, L. E.; Dunkelberger, E. B.; Zanni, M. T. Utilizing Lifetimes to Suppress Random Coil Features in 2D IR Spectra of Peptides. *J. Phys. Chem. Lett.* **2011**, *2*, 2357–2361.
- (14) Axelsen, P. H.; Kaufman, B. K.; McElhaney, R. N.; Lewis, R. N. A. H. The Infrared Dichroism of Transmembrane Helical Polypeptides. *Biophys. J.* **1995**, *69*, 2770–2781.
- (15) Bechinger, B.; Ruyschaert, J.-M.; Goormaghtigh, E. Membrane Helix Orientation from Linear Dichroism of Infrared Attenuated Total Reflection Spectra. *Biophys. J.* **1999**, *76*, 552–563.
- (16) Marsh, D.; Müller, M.; Schmitt, F. Orientation of the Infrared Transition Moments for an  $\alpha$ -Helix. *Biophys. J.* **2000**, *78*, 2499–2510.
- (17) Chen, X.; Wang, J.; Sniadecki, J. J.; Even, M. A.; Chen, Z. Probing  $\alpha$ -Helical and  $\beta$ -Sheet Structures of Peptides at Solid/Liquid Interfaces with SFG. *Langmuir* **2005**, *21*, 2662–2664.
- (18) Nguyen, K. T.; King, J. T.; Chen, Z. Orientation Determination of Interfacial  $\beta$ -Sheet Structures in Situ. *J. Phys. Chem. B* **2010**, *114*, 8291–8300.
- (19) Ye, S.; Nguyen, K. T.; Chen, Z. Interactions of Alamethicin with Model Cell Membranes Investigated Using Sum Frequency Generation Vibrational Spectroscopy in Real Time in Situ. *J. Phys. Chem. B* **2010**, *114*, 3334–3340.
- (20) Shen, Y. R. Surface Properties Probed by Second-Harmonic and Sum-Frequency Generation. *Nature* **1989**, *337*, 519–525.
- (21) Du, Q.; Superfine, R.; Freysz, E.; Shen, Y. R. Vibrational Spectroscopy of Water at the Vapor/Water Interface. *Phys. Rev. Lett.* **1993**, *70*, 2313–2316.
- (22) Du, Q.; Freysz, E.; Shen, Y. R. Surface Vibrational Spectroscopic Studies of Hydrogen Bonding and Hydrophobicity. *Science* **1994**, *264*, 826–828.
- (23) Eisenthal, K. B. Liquid Interfaces Probed by Second-Harmonic and Sum-Frequency Spectroscopy. *Chem. Rev.* **1996**, *96*, 1343–1360.
- (24) Chen, X.; Chen, Z. SFG Studies on Interactions Between Antimicrobial Peptides and Supported Lipid Bilayers. *Biochim. Biophys. Acta* **2006**, *1758*, 1257–1273.
- (25) Sovago, M.; Campen, R. K.; Wurfel, G. W. H.; Müller, M.; Bakker, H. J.; Bonn, M. Vibrational Response of Hydrogen-Bonded Interfacial Water is Dominated by Intramolecular Coupling. *Phys. Rev. Lett.* **2008**, *100*, 173901–1–173901-4.
- (26) Jungwirth, P.; Winter, B. Ions at Aqueous Interfaces: From Water Surface to Hydrated Proteins. *Annu. Rev. Phys. Chem.* **2008**, *59*, 343–366.
- (27) Ye, S.; Nguyen, K. T.; Clair, S. V. L.; Chen, Z. In Situ Molecular Level Studies on Membrane Related Peptides and Proteins in Real Time Using Sum Frequency Generation Vibrational Spectroscopy. *J. Struct. Biol.* **2009**, *168*, 61–77.
- (28) Bonn, M.; Campen, R. K. Optical Methods for the Study of Dynamics in Biological Membrane Models. *Surf. Sci.* **2009**, *603*, 1945–1952.
- (29) Weidner, T.; Apte, J. S.; Gamble, L. J.; Castner, D. G. Probing the Orientation and Conformation of  $\alpha$ -Helix and  $\beta$ -Strand Model Peptides on Self-Assembled Monolayers Using Sum Frequency Generation and NEXAFS Spectroscopy. *Langmuir* **2010**, *26*, 3433–3440.
- (30) Boughton, A. P.; Andricioaei, I.; Chen, Z. Surface Orientation of Magainin 2: Molecular Dynamics Simulation and Sum Frequency Generation Vibrational Spectroscopic Studies. *Langmuir* **2010**, *26*, 16031–16036.
- (31) Fu, L.; Ma, G.; Yan, E. C. Y. In Situ Misfolding of Human Islet Amyloid Polypeptide at Interfaces Probed by Vibrational Sum Frequency Generation. *J. Am. Chem. Soc.* **2010**, *132*, 5405–5412.
- (32) Fu, L.; Liu, J.; Yan, E. C. Y. Chiral Sum Frequency Generation Spectroscopy for Characterizing Protein Secondary Structures at Interfaces. *J. Am. Chem. Soc.* **2011**, *133*, 8094–8097.
- (33) Fu, L.; Wang, Z.; Yan, E. C. Chiral Vibrational Structures of Proteins at Interfaces Probed by Sum Frequency Generation Spectroscopy. *Int. J. Mol. Sci.* **2011**, *12*, 9404–9425.
- (34) Boughton, A. P.; Nguyen, K.; Andricioaei, I.; Chen, Z. Interfacial Orientation and Secondary Structure Change in Tachyplesin I: Molecular Dynamics and Sum Frequency Generation Spectroscopy Studies. *Langmuir* **2011**, *27*, 14343–14351.
- (35) Liu, Y.; Jasensky, J.; Chen, Z. Molecular Interactions of Proteins and Peptides at Interfaces Studied by Sum Frequency Generation Vibrational Spectroscopy. *Langmuir* **2012**, *28*, 2113–2121.
- (36) Yang, P.; Homan, A. B. K. T.; Tesmer, J. J. G.; Chen, Z. Membrane Orientation of  $G\alpha\beta_1\gamma_2$  and  $G\beta_1\gamma_2$  Determined Via Combined Vibrational Spectroscopic Studies. *J. Am. Chem. Soc.* **2013**, *135*, 5044–5051.
- (37) Liu, Y.; Ogorzalek, T. L.; Yang, P.; Schroeder, M. M.; Marsh, E. N. G.; Chen, Z. Molecular Orientation of Enzymes Attached to Surfaces Through Defined Chemical Linkages at the Solid-Liquid Interface. *J. Am. Chem. Soc.* **2013**, *135*, 12660–12669.
- (38) Lee, C. M.; Mohamed, N. M. A.; Watts, H. D.; Kubicki, J. D.; Kim, S. H. Sum-Frequency-Generation Vibration Spectroscopy and Density Functional Theory Calculations with Dispersion Corrections (DFT-D2) for Cellulose Ia and Ib. *J. Phys. Chem. B* **2013**, *117*, 6681–6692.

- (39) Chen, X.; Wang, J.; Boughton, A. P.; Kristalyn, C. B.; Chen, Z. Multiple Orientation of Melittin Inside a Single Lipid Bilayer Determined by Combined Vibrational Spectroscopic Studies. *J. Am. Chem. Soc.* **2007**, *129*, 1420–1427.
- (40) Chen, X.; Boughton, A. P.; Tesmer, J. J. G.; Chen, Z. In Situ Investigation of Heterotrimeric G Protein  $\beta\gamma$  Subunit Binding and Orientation on Membrane Bilayers. *J. Am. Chem. Soc.* **2007**, *129*, 12658–12659.
- (41) Ye, S.; Li, H.; Wei, F.; Jasensky, J.; Boughton, A. P.; Yang, P.; Chen, Z. Observing a Model Ion Channel Gating Action in Model Cell Membranes in Real Time in Situ: Membrane Potential Change Induced Alamethicin Orientation Change. *J. Am. Chem. Soc.* **2012**, *134*, 6237–6243.
- (42) Wei, F.; Ye, S.; Li, H.; Luo, Y. Phosphate Ions Promoting Association Between Peptide and Modeling Cell Membrane Revealed by Sum Frequency Generation Vibrational Spectroscopy. *J. Phys. Chem. C* **2013**, *117*, 11095–11103.
- (43) Fu, L.; Xiao, D.; Wang, Z.; Batista, V. S.; Yan, E. C. Y. Chiral Sum Frequency Generation for in Situ Probing Proton Exchange in Antiparallel  $\beta$ -Sheets at Interfaces. *J. Am. Chem. Soc.* **2013**, *135*, 3592–3598.
- (44) Wang, Z.; Fu, L.; Yan, E. C. Y. C-H stretch for Probing Kinetics of Self-Assembly into Macromolecular Chiral Structures at Interfaces by Chiral Sum Frequency Generation Spectroscopy. *Langmuir* **2013**, *29*, 4077–4083.
- (45) Lin, Y.-S.; Shorb, J. M.; Mukherjee, P.; Zanni, M. T.; Skinner, J. L. Empirical Amide I Vibrational Frequency Map: Application to 2D-IR Line Shapes for Isotope-Edited Membrane Peptide Bundles. *J. Phys. Chem. B* **2009**, *113*, 592–602.
- (46) Reddy, A. S.; Wang, L.; Lin, Y.-S.; Ling, Y.; Chopra, M.; Zanni, M. T.; Skinner, J. L.; de Pablo, J. J. Solution Structures of Rat Amylin Peptide: Simulation, Theory and Experiment. *Biophys. J.* **2010**, *98*, 443–451.
- (47) Reddy, A. S.; Wang, L.; Singh, S.; Ling, Y. L.; Buchanan, L.; Zanni, M. T.; Skinner, J. L.; de Pablo, J. J. Stable and Metastable States of Human Amylin in Solution. *Biophys. J.* **2010**, *99*, 2208–2216.
- (48) Wang, L.; Middleton, C. T.; Zanni, M. T.; Skinner, J. L. Development and Validation of Transferable Amide I Vibrational Frequency Maps for Peptides. *J. Phys. Chem. B* **2011**, *115*, 3713–3724.
- (49) Wang, L.; Middleton, C. T.; Singh, S.; Reddy, A. S.; Woys, A. M.; Strasfeld, D. B.; Marek, P.; Raleigh, D. P.; de Pablo, J. J.; Zanni, M. T.; et al. 2DIR Spectroscopy of Human Amylin Fibrils Reflects Stable  $\beta$ -Sheet Structure. *J. Am. Chem. Soc.* **2011**, *133*, 16062–16071.
- (50) Middleton, C. T.; Marek, P.; Cao, P.; Chiu, C.; Singh, S.; Woys, A. M.; de Pablo, J. J.; Raleigh, D. P.; Zanni, M. T. Two-Dimensional Infrared Spectroscopy Reveals the Complex Behaviour of an Amyloid Fibril Inhibitor. *Nat. Chem.* **2012**, *4*, 355–360.
- (51) Wang, L.; Skinner, J. L. Thermally-Induced Protein Unfolding Probed by Isotope-Edited IR Spectroscopy. *J. Phys. Chem. B* **2012**, *116*, 9627–9634.
- (52) Clarke, M. L.; Wang, J.; Chen, Z. Conformational Changes of Fibrinogen After Adsorption. *J. Phys. Chem. B* **2005**, *109*, 22027–22035.
- (53) Shen, Y. R. *The Principles of Nonlinear Optics*; Wiley-Interscience: Hoboken, NJ, 2003.
- (54) Boyd, R. W. *Nonlinear Optics*, 2nd ed.; Academic Press: San Diego, 2003.
- (55) Hirose, C.; Akamatsu, N.; Domen, K. Formulas for the Analysis of the Surface SFG Spectrum and Transformation Coefficients of Cartesian SFG Tensor Components. *Appl. Spectrosc.* **1992**, *46*, 1051–1072.
- (56) Zhuang, X.; Miranda, P. B.; Kim, D.; Shen, Y. R. Mapping Molecular Orientation and Conformation at Interfaces by Surface Nonlinear Optics. *Phys. Rev. B* **1999**, *59*, 12632–12640.
- (57) Raymond, E. A.; Tarbuck, T. L.; Richmond, G. L. Isotopic Dilution Studies of the Vapor/Water Interface as Investigated by Vibrational Sum-Frequency Spectroscopy. *J. Phys. Chem. B* **2002**, *106*, 2817–2820.
- (58) Raymond, E. A.; Tarbuck, T. L.; Brown, M. G.; Richmond, G. L. Hydrogen Bonding Interactions at the Vapor/Water Interface Investigated by Vibrational Sum-Frequency Spectroscopy of HOD/H<sub>2</sub>O/D<sub>2</sub>O Mixtures and Molecular Dynamics Simulations. *J. Phys. Chem. B* **2003**, *107*, 546–556.
- (59) Wang, H.-F.; Gan, W.; Lu, R.; Rao, Y.; Wu, B.-H. Quantitative Spectral and Orientational Analysis in Surface Sum Frequency Generation Vibrational Spectroscopy (SFG-VS). *Int. Rev. Phys. Chem.* **2005**, *24*, 191–256.
- (60) Nguyen, K. T.; Clair, S. V. L.; Ye, S.; Chen, Z. Orientation Determination of Protein Helical Secondary Structures Using Linear and Nonlinear Vibrational Spectroscopy. *J. Phys. Chem. B* **2009**, *113*, 12169–12180.
- (61) Ye, S.; Li, H.; Yang, W.; Luo, Y. Accurate Determination of Interfacial Protein Secondary Structure by Combining Interfacial-Sensitive Amide I and Amide III Spectral Signals. *J. Am. Chem. Soc.* **2014**, *136*, 1206–1209.
- (62) Han, X.; Liu, Y.; Wu, F.-G.; Jansensky, J.; Kim, T.; Wang, Z.; C. L. Brooks, I.; Wu, J.; Xi, C.; Mello, C. M.; et al. Different Interfacial Behaviors of Peptides Chemically Immobilized on Surfaces with Different Linker Lengths and Via Different Termini. *J. Phys. Chem. B* **2014**, *118*, 2904–2912.
- (63) Giordmaine, J. A. Nonlinear Optical Properties of Liquids. *Phys. Rev.* **1965**, *138*, A1599–A1606.
- (64) Belkin, M. A.; Kulakov, T. A.; Ernst, J.-H.; Yan, L.; Shen, Y. R. Sum-Frequency Vibrational Spectroscopy on Chiral Liquids: A Novel Technique to Probe Molecular Chirality. *Phys. Rev. Lett.* **2000**, *85*, 4474–4477.
- (65) Wang, J.; Chen, X.; Clarke, M. L.; Chen, Z. Detection of Chiral Sum Frequency Generation Vibrational Spectra of Proteins and Peptides at Interfaces in Situ. *Proc. Natl. Acad. Sci. U.S.A.* **2005**, *102*, 4978–4983.
- (66) Xiao, D.; Fu, L.; Liu, J.; Batista, V. S.; Yan, E. C. Y. Amphiphilic Adsorption of Human Islet Amyloid Polypeptide Aggregates to Lipid/Aqueous Interfaces. *J. Mol. Biol.* **2012**, *421*, 537–547.
- (67) Perry, J. M.; Moad, A. J.; Begue, N. J.; Wampler, R. D.; Simpson, G. J. Electronic and Vibrational Second-Order Nonlinear Optical Properties of Protein Secondary Structural Motifs. *J. Phys. Chem. B* **2005**, *109*, 20009–20026.
- (68) Hauptert, L. M.; Simpson, G. J. Chirality in Nonlinear Optics. *Annu. Rev. Phys. Chem.* **2009**, *60*, 345–365.
- (69) Weidner, T.; Breen, N. F.; Li, K.; Drobny, G. P.; Castner, D. G. Sum Frequency Generation and Solid-State NMR Study of the Structure, Orientation, and Dynamics of Polystyrene-Adsorbed Peptides. *Proc. Natl. Acad. Sci. U.S.A.* **2010**, *107*, 13288–13293.
- (70) Ding, B.; Laaser, J. E.; Liu, Y.; Wang, P.; Zanni, M. T.; Chen, Z. Site-Specific Orientation of an  $\alpha$ -Helical Peptide Ovispirin-1 from Isotope Labeled SFG Spectroscopy. *J. Phys. Chem. B* **2013**, *117*, 14625–14634.
- (71) Simpson, G. J. Molecular Origins of the Remarkable Chiral Sensitivity of Second-Order Nonlinear Optics. *ChemPhysChem* **2004**, *5*, 1301–1310.
- (72) Liang, C.; Louhivuori, M.; Marrink, S. J.; Jansen, T. L. C.; Knoester, J. Vibrational Spectra of a Mechanosensitive Channel. *J. Phys. Chem. Lett.* **2013**, *4*, 448–452.
- (73) Liang, C.; Jansen, T. L. C. Simulation of Two-Dimensional Sum-Frequency Generation Response Functions: Application to Amide I in Proteins. *J. Phys. Chem. B* **2013**, *117*, 6937–6945.
- (74) Roeters, S. J.; van Dijk, C. N.; Torres-Knoop, A.; Backus, E. H. G.; Campen, R. K.; Bonn, M.; Woutersen, S. Determining in Situ Protein Conformation and Orientation from the Amide-I Sum-Frequency Generation Spectrum: Theory and Experiment. *J. Phys. Chem. A* **2013**, *117*, 6311–6322.
- (75) Buchanan, L. E.; Carr, J. K.; Fluitt, A. M.; Hoganson, A. J.; Moran, S. D.; de Pablo, J. J.; Skinner, J. L.; Zanni, M. T. Structural Motif of Polyglutamine Amyloid Fibrils Discerned with Mixed-Isotope Infrared Spectroscopy. *Proc. Natl. Acad. Sci. U.S.A.* **2014**, *111*, 5796–5801.

- (76) Hull, S. E.; Karlsson, R.; Main, P.; Woolfson, M. M.; Dodson, E. J. The Crystal Structure of a Hydrated Gramicidin S–Urea Complex. *Nature* **1978**, *275*, 206–207.
- (77) Krauss, E. M.; Chan, S. I. Spectroscopic Studies of Intramolecular Hydrogen Bonding in Gramicidin S. *J. Am. Chem. Soc.* **1982**, *104*, 1824–1830.
- (78) Smith, A. W.; Tokmakoff, A.; Amide, I. Two-Dimensional Infrared Spectroscopy of  $\beta$ -Hairpin Peptides. *J. Chem. Phys.* **2007**, *126*, 045109–1–045109–11.
- (79) Kupser, P.; Pagel, K.; Oomens, J.; Polfer, N.; Koks, B.; Meijer, G.; von Helden, G. Amide-I and -II Vibrations of the Cyclic  $\beta$ -Sheet Model Peptide Gramicidin S in the Gas Phase. *J. Am. Chem. Soc.* **2010**, *132*, 2085–2093.
- (80) Joshi, K.; Semrouni, D.; Ohanessian, G.; Clavaguera, C. Structure and IR Spectra of the Gramicidin S Peptide: Pushing the Quest for Low-Energy Conformations. *J. Phys. Chem. B* **2012**, *116*, 483–490.
- (81) Auer, B. M.; Skinner, J. L. Vibrational Sum-Frequency Spectroscopy of the Liquid/Vapor Interface for Dilute HOD in D<sub>2</sub>O. *J. Chem. Phys.* **2008**, *129*, 214705–1–214705–14.
- (82) Auer, B. M.; Skinner, J. L. Water: Hydrogen Bonding and Vibrational Spectroscopy, in the Bulk Liquid and at the Liquid/Vapor Interface. *Chem. Phys. Lett.* **2009**, *470*, 13–20.
- (83) Auer, B. M.; Skinner, J. L. Vibrational Sum-Frequency Spectroscopy of the Water Liquid/Vapor Interface. *J. Phys. Chem. B* **2009**, *113*, 4125–4130.
- (84) Torii, H.; Tasumi, M. Model Calculations on the Amide-I Infrared Bands of Globular Proteins. *J. Chem. Phys.* **1992**, *96*, 3379–3387.
- (85) Torii, H.; Tasumi, T.; Kanazawa, T.; Tasumi, M. Effects of Intermolecular Hydrogen-Bonding Interactions on the Amide I Mode of *N*-Methylacetamide: Matrix-Isolation Infrared Studies and ab Initio Molecular Orbital Calculations. *J. Phys. Chem. B* **1998**, *102*, 309–314.
- (86) Torii, H. In *Atoms, Molecules and Clusters in Electric Fields. Theoretical Approaches to the Calculation of Electric Polarizability*; Maroulis, G., Ed.; Imperial College Press: London, 2006; pp 179–214.
- (87) Torii, H. Nature of Vibrational Frequency Modulations and the Related One- and Two-Dimensional Vibrational Spectral Features Analysed for the Amide I Mode of Tetraalanine in Aqueous Solution. *Mol. Phys.* **2009**, *107*, 1855–1866.
- (88) Schmidt, J. R.; Corcelli, S. A.; Skinner, J. L. Ultrafast Vibrational Spectroscopy of Water and Aqueous *N*-Methylacetamide: Comparison of Different Electronic Structure/Molecular Dynamics Approaches. *J. Chem. Phys.* **2004**, *121*, 8887–8896.
- (89) Schmidt, J. R.; Corcelli, S. A.; Skinner, J. L. Pronounced Non-Condon Effects in the Ultrafast Infrared Spectroscopy of Water. *J. Chem. Phys.* **2005**, *123*, 044513–1–044513–13.
- (90) Auer, B. M.; Kumar, R.; Schmidt, J. R.; Skinner, J. L. Hydrogen Bonding and Raman, IR, and 2D-IR Spectroscopy of Dilute HOD in Liquid D<sub>2</sub>O. *Proc. Natl. Acad. Sci. U.S.A.* **2007**, *104*, 14215–14220.
- (91) Auer, B. M.; Skinner, J. L. Dynamical Effects in Line Shapes for Coupled Chromophores: Time-Averaging Approach. *J. Chem. Phys.* **2007**, *127*, 104105–1–104105–10.
- (92) Auer, B. M.; Skinner, J. L. IR and Raman Spectra of Liquid Water: Theory and Interpretation. *J. Chem. Phys.* **2008**, *128*, 224511–1–224511–12.
- (93) Skinner, J. L. Vibrational Line Shapes and Spectral Diffusion in Fluids. *Mol. Phys.* **2010**, *106*, 2245–2253.
- (94) Manor, J.; Mukherjee, P.; Lin, Y.-S.; Leonov, H.; Skinner, J. L.; Zanni, M. T.; Arkin, I. T. Gating Mechanism of the Influenza A M2 Channel Revealed by 1D and 2D Spectroscopies. *Structure* **2009**, *17*, 247–254.
- (95) Pieniazek, P. A.; Tainter, C. J.; Skinner, J. L. Surface of liquid water: Three-Body Interactions and Vibrational Sum-Frequency Spectroscopy. *J. Am. Chem. Soc.* **2011**, *133*, 10360–10363.
- (96) Pieniazek, P. A.; Tainter, C. J.; Skinner, J. L. Interpretation of the Water Surface Vibrational Sum-Frequency Spectrum. *J. Chem. Phys.* **2011**, *135*, 044701–1–044701–12.
- (97) Skinner, J. L.; Pieniazek, P. A.; Gruenbaum, S. M. Vibrational Spectroscopy of Water at Interfaces. *Acc. Chem. Res.* **2012**, *45*, 93–100.
- (98) Mukherjee, P.; Krummel, A. T.; Fulmer, E. C.; Kass, I.; Arkin, I. T.; Zanni, M. T. Site-Specific Vibrational Dynamics of the CD3 $\zeta$  Membrane Peptide Using Heterodyned Two-Dimensional Infrared Photon Echo Spectroscopy. *J. Chem. Phys.* **2004**, *120*, 10215–10224.
- (99) Torii, H.; Tasumi, M. Ab Initio Molecular Orbital Study of the Amide I Vibrational Interactions Between the Peptide Groups in Di- and Tripeptides and Considerations on the Conformation of the Extended Helix. *J. Raman Spectrosc.* **1998**, *29*, 81–86.
- (100) Jansen, T. L. C.; Dijkstra, A. G.; Watson, T. M.; Hirst, J. D.; Knoester, J. Modeling the Amide I Bands of Small Peptides. *J. Chem. Phys.* **2006**, *125*, 044312–1–044312–9.
- (101) Roy, S.; Lessing, J.; Meisl, G.; Ganim, Z.; Tokmakoff, A.; Knoester, J.; Jansen, T. L. C. Solvent and Conformation Dependence of Amide I Vibrations in Peptides and Proteins Containing Proline. *J. Chem. Phys.* **2011**, *135*, 234507–1–234507–11.
- (102) Tsuboi, M.; Ikeda, T.; Ueda, T. Raman Microscopy of a Small Uniaxial Crystal: Tetragonal Aspartame. *J. Raman Spectrosc.* **1991**, *22*, 619–626.
- (103) Laaser, J. E.; Zanni, M. T. Extracting Structural Information from the Polarization Dependence of One- and Two-Dimensional Sum Frequency Generation Spectra. *J. Phys. Chem. A* **2013**, *117*, 5875–5890.
- (104) McQuarrie, D. A. *Statistical Mechanics*; Harper and Row: New York, 1976.
- (105) Schmidt, J. R.; Roberts, S. T.; Loparo, J. J.; Tokmakoff, A.; Fayer, M. D.; Skinner, J. L. Are Water Simulation Models Consistent with Steady-State and Ultrafast Vibrational Spectroscopy Experiments? *Chem. Phys.* **2007**, *341*, 143–157.
- (106) Chen, X. G.; Schweitzer-Stenner, R.; Asher, S. A.; Mirkin, N. G.; Krimm, S. Vibrational Assignments of *Trans-N*-Methylacetamide and Some of Its Deuterated Isotopomers from Band Decomposition of IR, Visible, and Resonance Raman Spectra. *J. Phys. Chem.* **1995**, *99*, 3074–3083.
- (107) Hess, B.; Kutzner, C.; van der Spoel, D.; Lindahl, E. GROMACS 4: Algorithms for Highly Efficient, Load-Balanced, and Scalable Molecular Simulation. *J. Chem. Theor. Comput.* **2008**, *4*, 435–447.
- (108) Oostenbrink, C.; Villa, A.; Mark, A. E.; van Gunsteren, W. F. A Biomolecular Force Field Based on the Free Enthalpy of Hydration and Solvation: The GROMOS Force-Field Parameter Sets 53A5 and 53A6. *J. Comput. Chem.* **2004**, *25*, 1656–1676.
- (109) Berendsen, H. J. C.; Postma, J. P. M.; van Gunsteren, W. F.; Hermans, J. In *Intermolecular Forces*; Pullman, B., Ed.; Reidel: Dordrecht, 1981.
- (110) Berendsen, H. J. C.; Postma, J. P. M.; van Gunsteren, W. F.; DiNola, A.; Haak, J. R. Molecular Dynamics with Coupling to an External Bath. *J. Chem. Phys.* **1984**, *81*, 3684–3690.
- (111) Nosé, S. A Unified Formulation of the Constant Temperature Molecular Dynamics Methods. *J. Chem. Phys.* **1984**, *81*, 511–519.
- (112) Hoover, W. G. Canonical Dynamics – Equilibrium Phase-Space Distributions. *Phys. Rev. A* **1985**, *31*, 1695–1697.
- (113) Welch, W. R. W.; Kubelka, J.; Keiderling, T. A. Infrared, Vibrational Circular Dichroism, and Raman Spectral Simulations for  $\beta$ -sheet Structures with Various Isotopic Labels, Interstrand, and Stacking Arrangements Using Density Functional Theory. *J. Phys. Chem. B* **2013**, *117*, 10343–10358.
- (114) Wampler, R. D.; Zhou, M.; Thompson, D. H.; Simpson, G. J. Mechanism of the Chiral SHG Activity of Bacteriorhodopsin Films. *J. Am. Chem. Soc.* **2006**, *128*, 10994–10995.
- (115) Ji, N.; Ostroverkhov, V.; Chen, C.-Y.; Shen, Y.-R. Phase-Sensitive Sum-Frequency Vibrational Spectroscopy and Its Application to Studies of Interfacial Alkyl Chains. *J. Am. Chem. Soc.* **2007**, *129*, 10056–10057.
- (116) Stiofkin, I. V.; Jayathilake, H. D.; Bordenyuk, A. N.; Benderskii, A. V. Heterodyne-Detected Vibrational Sum Frequency Generation Spectroscopy. *J. Am. Chem. Soc.* **2008**, *130*, 2271–2275.



- (117) Stiopkin, I. V.; Weeraman, C.; Pieniazek, P. A.; Shalhout, F. Y.; Skinner, J. L.; Benderskii, A. V. Hydrogen Bonding at the Water Surface Revealed by Isotopic Dilution Spectroscopy. *Nature* **2011**, *474*, 192–195.
- (118) Laaser, J. E.; Xiong, W.; Zanni, M. T. Time-Domain SFG Spectroscopy Using Mid-IR Pulse Shaping: Practical and Intrinsic Advantages. *J. Phys. Chem. B* **2011**, *115*, 2536–2546.
- (119) Laaser, J. E.; Sko, D. R.; Ho, J.-J.; Joo, Y.; Serrano, A. L.; Steinkruger, J. D.; Gopalan, P.; Gellman, S. H.; Zanni, M. T. Two-Dimensional Sum-Frequency Generation Reveals Structure and Dynamics of a Surface-Bound Peptide. *J. Am. Chem. Soc.* **2014**, *136*, 956–962.
- (120) Torres, J.; Adams, P. D.; Arkin, I. T. Use of a New Label,  $^{13}\text{C}=^{18}\text{O}$ , in the Determination of a Structural Model of Phospholamban in a Lipid Bilayer. Spatial Constraints Resolve the Ambiguity Arising from Interpretations of Mutagenesis Data. *J. Mol. Biol.* **2000**, *300*, 677–685.
- (121) Torres, J.; Kukol, A.; Goodman, J. M.; Arkin, I. T. Site-Specific Examination of Secondary Structure and Orientation Determination in Membrane Proteins: The Peptidic  $^{13}\text{C}=^{18}\text{O}$  Group as a Novel Infrared Probe. *Biopolymers* **2001**, *59*, 396–401.
- (122) Fang, C.; Wang, J.; Charnley, A. K.; Barber-Armstrong, W.; Smith, A. B.; Decatur, S. M.; Hochstrasser, R. M. Two-Dimensional Infrared Measurements of the Coupling Between Amide Modes of an  $\alpha$ -Helix. *Chem. Phys. Lett.* **2003**, *382*, 586–592.
- (123) Fang, C.; Wang, J.; Kim, Y. S.; Charnley, A. K.; Barber-Armstrong, W.; Smith, A. B.; Decatur, S. M.; Hochstrasser, R. M. Two-Dimensional Infrared Spectroscopy of Isotopomers of an Alanine Rich  $\alpha$ -Helix. *J. Phys. Chem. B* **2004**, *108*, 10415–10427.
- (124) Fang, C.; Hochstrasser, R. M. Two-Dimensional Infrared Spectra of the  $^{13}\text{C}=^{18}\text{O}$  Isotopomers of Alanine Residues in an  $\alpha$ -Helix. *J. Phys. Chem. B* **2005**, *109*, 18652–18663.
- (125) Arkin, I. T. Isotope-Edited IR Spectroscopy for the Study of Membrane Proteins. *Curr. Opin. Chem. Biol.* **2006**, *10*, 394–401.
- (126) Brewer, S. H.; Song, B.; Raleigh, D. P.; Dyer, R. B. Residue Specific Resolution of Protein Folding Dynamics Using Isotope-Edited Infrared Temperature Jump Spectroscopy. *Biochemistry* **2007**, *46*, 3279–3285.
- (127) Decatur, S. M. Elucidation of Residue-Level Structure and Dynamics of Polypeptides Via Isotope-Edited Infrared Spectroscopy. *Acc. Chem. Res.* **2006**, *39*, 169–175.
- (128) Mukherjee, P.; Kass, I.; Arkin, I.; Zanni, M. T. Picosecond Dynamics of a Membrane Protein Revealed by 2D IR. *Proc. Natl. Acad. Sci. U.S.A.* **2006**, *103*, 3528–3533.
- (129) Mukherjee, P.; Kass, I.; Arkin, I. T.; Zanni, M. T. Structural Disorder of the CD3 $\zeta$  Transmembrane Domain Studied with 2D IR Spectroscopy and Molecular Dynamics Simulation. *J. Phys. Chem. B* **2006**, *110*, 24740–24749.
- (130) Shim, S.-H.; Gupta, R.; Ling, Y. L.; Strasfeld, D. B.; Raleigh, D. P.; Zanni, M. T. Two-Dimensional IR Spectroscopy and Isotope Labeling Defines the Pathway of Amyloid Formation with Residue Specific Resolution. *Proc. Natl. Acad. Sci. U.S.A.* **2009**, *106*, 6614–6619.
- (131) Nagarajan, S.; Taskent-Sezgin, H.; Parul, D.; Carrico, I.; Raleigh, D. P.; Dyer, R. B. Differential Ordering of the Protein Backbone and Side Chains During Protein Folding Revealed by Site-Specific Recombinant Infrared Probes. *J. Am. Chem. Soc.* **2011**, *133*, 20335–20340.
- (132) Goldstein, H. *Classical Mechanics*; Addison-Wesley: Reading, MA, 1980.